

## Momentum broadening of an in-medium jet evolution using a light-front Hamiltonian approach

Meijian Li<sup>1,2,3,\*</sup>, Tuomas Lappi<sup>1,2,†</sup>, Xingbo Zhao<sup>4,5,‡</sup> and Carlos A. Salgado<sup>3,§</sup>

<sup>1</sup>*Department of Physics, University of Jyväskylä, P.O. Box 35, FI-40014 Finland*

<sup>2</sup>*Helsinki Institute of Physics, University of Helsinki, P.O. Box 64, FI-00014 Finland*

<sup>3</sup>*Instituto Galego de Física de Altas Enerxías (IGFAE), Universidade de Santiago de Compostela, E-15782 Galicia, Spain*

<sup>4</sup>*Institute of Modern Physics, Chinese Academy of Sciences, Lanzhou 730000, China*

<sup>5</sup>*University of Chinese Academy of Sciences, Beijing 100049, China*



(Received 26 May 2023; accepted 21 July 2023; published 17 August 2023)

Following the nonperturbative light-front Hamiltonian formalism developed in our preceding work [Li *et al.* *Phys. Rev. D* **104**, 056014 (2021)], we investigate the momentum broadening of a quark jet inside a SU(3) colored medium. We perform the numerical simulation of the real-time jet evolution in Fock spaces of a single quark, a quark-gluon state, and coupled quark- and quark-gluon states at various jet momenta  $p^+$  and medium densities. With the obtained jet light-front wave function, we extract the jet transverse momentum distribution, the quenching parameter, and the gluon emission rate. We analyze the dependence of momentum broadening on  $p^+$ , medium density, color configuration, spatial correlation, and medium-induced gluon emission. For comparison, we also derive analytically the expectation value of the transverse momentum of a quark-gluon state in any color configuration and in an arbitrary spatial distribution in the eikonal limit. This work can help understand jet momentum broadening in the noneikonal regime.

DOI: [10.1103/PhysRevD.108.036016](https://doi.org/10.1103/PhysRevD.108.036016)

### I. INTRODUCTION

A central goal of ultrarelativistic heavy ion collisions, such as those performed at the Relativistic Heavy-Ion Collider and the LHC, is to recreate droplets of matter in the early Universe, the quark-gluon plasma, and learn about its properties [1]. In heavy-ion collisions, energetic quarks and gluons are produced at early stages, propagating through the dense and hot medium. The initial particle is transformed into a cone-shaped beam of hadrons, a jet. In theoretical studies, a jet initiated by a high energy quark(gluon) is often referred to as the quark(gluon) jet. Experimentally, the energy and motion of the original particle are estimated by measuring the hadrons in the jet. The jets are suppressed and modified compared to those in proton-proton collisions, a phenomenon known as jet quenching, observed at the Relativistic Heavy-Ion Collider [2–5] and the LHC [6–8].

Similar processes happen in deeply inelastic scattering, where jets lose energy when traversing the cold nuclear matter formed from the large nucleus.

Studies of jet quenching give us information on how the medium responds when traversed by a high-energy quark or gluon jet, and how the jet is modified by the medium [9–15]. Several perturbative-QCD-based studies have been carried out to calculate jet energy loss through multiple scatterings and gluon radiations. In the Baier-Dokshitzer-Mueller-Peigne-Schiff and Zakharov approach, the medium is modeled as a collection of static scattering centers and soft gluon radiations are induced through multiple scatterings [16–18]. Gyulassy-Levai-Vitev and Wiedemann [19–21] developed a systematic expansion of the calculation in terms of the number of scatterings. In the Arnold, Moore, and Yaffe [22,23] approach, the hard thermal loop framework is employed and the medium is treated as in a thermal equilibrium state. In the higher-twist approach, the twist-expansion is used in a collinear factorization formalism and the medium is characterized by matrix elements of gauge field operators [24,25]. In the SCETG formalism [26,27], the standard soft collinear effective theory Lagrangian is modified to include Glauber modes of gluon field for parton interactions.

In preceding works, we have developed a computational method of simulating the evolution of a quark jet inside a classical color background field, first

\*meijian.li@usc.es

†tuomas.v.v.lappi@jyu.fi

‡xbzhao@impcas.ac.cn

§carlos.salgado@usc.es

Published by the American Physical Society under the terms of the [Creative Commons Attribution 4.0 International license](https://creativecommons.org/licenses/by/4.0/). Further distribution of this work must maintain attribution to the author(s) and the published article's title, journal citation, and DOI. Funded by SCOAP<sup>3</sup>.

in the  $|q\rangle$  Fock sector [28], then in the  $|q\rangle + |qg\rangle$  Fock sector [29]. This method is known as the time-dependent basis light-front quantization (tBLFQ) [30], a light-front Hamiltonian formalism. Unlike the aforementioned perturbative-QCD-based approaches, the evolution process is calculated on the amplitude rather than the probability level. This method enables us to relax approximations usually made in high-energy collisions, such as the eikonal and the collinear radiation approximations [15].

The tBLFQ method has also been applied to various problems in quantum electrodynamics [31–34], and its quantum mechanics counterpart—the time-dependent basis function approach to nuclear structure and scattering [35,36]. The advantages of the light-front Hamiltonian formalism are also used in a recent study in small- $x$  physics to study spin-related observables [37]. It is noteworthy that the tBLFQ (and the related time-dependent basis function) approach is well suited to be implemented as quantum simulations on a quantum device. Recent developments can be found in Refs. [38–41]. The calculation in this work, though performed on classical computers, also provides a precursor for the future implementation of quantum simulation, with the anticipation of a quantum speedup [42,43].

In this work, we present a study on the momentum broadening of in-medium jet evolution using tBLFQ. We aim to enhance the understanding of the mechanism in jet momentum broadening: the momentum exchange of the jet constituents with the medium and the effects from gluon radiation. The new development in this work answers the following key questions:

- (1) *How do we extract and interpret the momentum broadening from the jet's wave function formulated on a discrete momentum basis space?* We have shown that, in tBLFQ, the quark jet is described by an evolving light-front wave function, a superposition of different momenta, color, and helicity modes in the  $|q\rangle + |qg\rangle$  space, and we examine various observables and quantities from it [29]. To complement and further develop the study on the transverse momentum space, we extract the time-dependent transverse momentum square  $\langle \vec{p}_\perp^2(x^+) \rangle$  and the quenching parameter  $\hat{q}$  (defined in the next section) from the jet state. Importantly, one must understand the dependence on the physical and the basis parameters in simulations on a finite basis space, especially the infrared and ultraviolet cutoffs, which we will examine and elaborate on.
- (2) *What is the analytical expectation of the momentum broadening of the quark-gluon state at finite  $N_c$ , in the eikonal limit, given the state arbitrarily distributed in color and transverse space?* The analytical expression of  $\langle \vec{p}_\perp^2(x^+) \rangle$ , in terms of medium strength, momentum cutoffs, and evolution time, is known for the single particle state (the quark or gluon jet), derived with Wilson lines in the

McLerran-Venugopalan (MV) model [44–46]. But the result for the quark-gluon state is absent. We fill this gap by presenting the full derivation using the four-point  $\bar{q} \bar{g} qg$  Wilson line correlators. This result can be useful to other studies on jet quenching with quark-gluon components, for example, the production of the quark-gluon dijet in high-energy collisions, especially when one needs to look at color-differential cross sections [47–50]. Here, it also serves as a benchmark for checking the numerical simulations in the eikonal limit.

- (3) *What is the effect from the medium at finite  $p^+$  and finite  $N_\eta$  (number of uncorrelated medium layers, defined in the next section)?* The picture of jet quenching becomes very complicated when the eikonal approximation gets relaxed: at finite  $p^+$ , there is a diffusion in transverse coordinate space resulting from the kinetic energy part of the Hamiltonian, and there exists a continuous gluon emission/absorption throughout the evolution even when only allowing one dynamical gluon at the same time. In addition, to be more realistic, we also let the number of uncorrelated medium layers in the MV model, namely  $N_\eta$ , be finite. We will analyze those effects using the evolved jet wave function obtained from numerical simulations. We observe a suppression on  $\hat{q}$  at finite  $p^+$  and finite  $N_\eta$ . The medium enhances the gluon emission compared to the vacuum, but slows down the total momentum broadening of the quark jet state compared to a quark-gluon state.

We would like to clarify that in formulating the jet state in the  $|q\rangle + |qg\rangle$  Fock space, we use, as the initial state, a single  $|q\rangle$  state with definite momentum. This setup closely resembles the scenario where the quark is produced inside the medium from a hard scattering. It provides a simplified picture in studying effects of in-medium jet momentum broadening and favors the interpretation of physics in terms of single particles. It is important to note that this setup differs from the scenario where the quark originates from far outside the medium and is described by the light-front wave function of the QCD eigenstate in the truncated Fock space. Despite this distinction, the investigation carried out in this work is essential for future studies involving the latter scenario.

The layout of this paper is as follows. We first introduce the method in Sec. II. We then present and discuss the analytical results in the eikonal limit in Sec. III and the numerical results of the full nonperturbative calculation in Sec. IV. We conclude with a discussion of future steps beyond this work in Sec. V.

## II. METHODOLOGY

In Ref. [29], we have developed the formalism of using the tBLFQ approach to simulate the evolution of a quark jet

inside a classical color background field in the  $|q\rangle + |qg\rangle$  Fock sector. Here, we briefly review the basics of this formalism and reformulate the physical quantities in dimensionless variables.

### A. Jet evolution in tBLFQ

The light-front Hamiltonian consists of three parts,  $P^-(x^+) = P_{KE}^- + V_{qg} + V_{\mathcal{A}}(x^+)$ , which are the kinetic energy term, the gluon emission/absorption term, and the interaction term with a background field (the medium), respectively. The background field  $\mathcal{A}$  describing the medium is given by the MV model [44–46]. We refer to Ref. [29] for the derivation and the full expression of  $P^-$ . The evolution of the state is treated by decomposing the time-evolution operator into many small steps of the light-front time  $x^+$ , then solved in the time sequence numerically,

$$\begin{aligned} |\psi; x^+\rangle &= T_+ \exp \left[ -\frac{i}{2} \int_0^{x^+} dz^+ P^-(z^+) \right] |\psi; 0\rangle, \\ &= \lim_{n \rightarrow \infty} \prod_{k=1}^n T_+ \exp \left[ -\frac{i}{2} \int_{x_{k-1}^+}^{x_k^+} dz^+ P^-(z^+) \right] |\psi; 0\rangle, \end{aligned} \quad (1)$$

in which  $x_k^+ = k\delta x^+$  ( $k = 0, 1, 2, \dots, n$ ) with  $\delta x^+ \equiv x^+/n$ . The numerical method for this specific problem is optimized in Ref. [29]. That is, within each small time step, we treat  $P_{KE}^-$  and  $V_{\mathcal{A}}$  as time-constant operators and carry out matrix exponentiation in the momentum and coordinate space, respectively; the operation with  $V_{qg}$  uses the fourth-order Runge-Kutta method in momentum space.

The formulated basis space consists of a square lattice with periodic boundary conditions in the transverse dimensions  $\vec{x}_\perp$ , ranging in  $[-L_\perp, L_\perp]$  with  $2N_\perp$  sites, and a loop with (anti)periodic boundary condition in the  $x^-$  direction, of length  $2L$ , for the gluon (quark). The transverse lattice introduces a pair of infrared (IR) and ultraviolet (UV) cutoffs in the transverse momentum space  $\vec{p}_\perp$ ,  $\lambda_{\text{IR}} = d_p = \pi/L_\perp$  and  $\lambda_{\text{UV}} = \pi/a_\perp$ , with  $a_\perp = L_\perp/N_\perp$  as the lattice spacing. Therefore the simulations are performed at fixed IR and UV cutoffs, which means setting upper and lower bounds on the  $\int p_\perp$  integral in the corresponding analytical calculations. We will see later that the physical IR regulator  $m_g$  will play the role of the IR cutoff instead of  $\lambda_{\text{IR}}$ , but the UV cutoff is still the lattice-dependent  $\lambda_{\text{UV}}$ . To relate to a physical process, one needs to match such cutoffs to realistic momentum scales. For example, the study in Ref. [51] uses the Landau matching condition to choose cutoff models that depend on the jet energy and plasma temperature. In this work, we study the dependence of the jet observables at a range of cutoffs.

The longitudinal momentum  $p^+$  is quantized in units of  $2\pi/L$ , and the gluon(quark) is allowed to take a positive (half-)integer number in this unit. For the total momentum

of the quark jet state,  $K$  is a half-integer (note that  $K \geq 1.5$  in order to accommodate multiple  $p^+$  configurations for the  $|qg\rangle$  sector), with  $p^+ = K2\pi/L$  and  $p^+ = p_Q^+ = p_q^+ + p_g^+$ .<sup>1</sup> Then the longitudinal momentum fraction of the gluon,  $z \equiv p_g^+/p^+$ , has a resolution of  $1/K$ .

The total evolution time, which is also the thickness of the medium, is  $x^+ = [0, L_\eta]$ . The  $x^+$  dimension is discretized into small time steps of  $\delta x^+$  for numerically simulating the time evolution, as seen in Eq. (1). Meanwhile, the medium along  $x^+$  is discretized into a number of  $N_\eta$  uncorrelated layers such that each layer has a duration of  $\tau \equiv L_\eta/N_\eta$ . This layer structure is to numerically simulate the stochastic feature of the sources along  $x^+$  that generate the medium [52], characterized in continuum by the correlation relation

$$\langle \rho_a(\vec{x}_\perp, x^+) \rho_b(\vec{y}_\perp, y^+) \rangle_m = g^2 \tilde{\mu}^2 \delta_{ab} \delta^2(\vec{x}_\perp - \vec{y}_\perp) \delta(x^+ - y^+). \quad (2)$$

This continuum relation corresponds to the limit  $N_\eta \rightarrow \infty$  ( $\tau \rightarrow 0$ ), but we can keep  $\tau$  general and thus introduce a finite longitudinal correlation length into our description of the medium. The average over the medium configurations is indicated by  $\langle \dots \rangle_m$ . The medium color field  $\mathcal{A}$  is calculated from the sources by solving the reduced Yang-Mills equation with an IR regulator  $m_g$ ,

$$(m_g^2 - \nabla_\perp^2) \mathcal{A}_a^-(\vec{x}_\perp, x^+) = \rho_a(\vec{x}_\perp, x^+). \quad (3)$$

The details on how to simulate the medium in the basis space are discussed in Appendix A 2.

In this Hamiltonian formalism, the jet as a quantum state is described by its light-front wave function at different time instances. The wave function reads as a column vector of coefficients in the above-formulated basis space. For a given observable  $\hat{O}$ , one can directly evaluate its expectation value as  $\langle O(x^+) \rangle = \langle \psi; x^+ | \hat{O} | \psi; x^+ \rangle$ , using the jet wave function solved from a single simulation. Then, by taking the average of  $\langle O(x^+) \rangle$ s from multiple simulations, each with an independently sampled  $\rho$ , we arrive at the configuration averaged  $\langle O(x^+) \rangle_m$ .

### B. Parameter dependence

To have a qualitative understanding of how the physical process should depend on the parameters of the setup, here we consider the integrated Hamiltonian,  $P^-$  summed over the spatial dimensions  $(\vec{x}_\perp, x^-)$  and accumulated over a time duration of  $\Delta x^+$ . Let us examine the three terms individually.

<sup>1</sup>We use the subscripts “ $Q$ ” and “ $q$ ” to distinguish between the quark in the  $|q\rangle$  sector and that in the  $|qg\rangle$  sector.

First, for the kinetic energy term,  $P_{KE}^-$ , its effect as in the evolution operator mainly depends on three dimensionless quantities,

$$e^{-\frac{i}{2}P_{KE}^- \Delta x^+} \sim f \left[ \frac{2L\Delta x^+}{(2a_\perp)^2}, \frac{m_q a_\perp}{\pi}, \frac{1}{K} \right]. \quad (4)$$

The dependence on the first quantity in the product form is a result of the longitudinal boost invariance. In the view of the full evolution process, viz.,  $\Delta x^+ \rightarrow L_\eta$ , this action stays the same by scaling the  $p^+$  momentum (via inversely scaling  $L$ ) of the incoming quark and its evolution time  $L_\eta$  equally. The dependence on the second quantity reflects the contribution from the quark mass as compared to the largest transverse momentum mode  $\lambda_{UV}$ . The third quantity reflects the resolution in probing the longitudinal momentum fraction of the particle in the  $|qg\rangle$  sector.

Second, the gluon emission/absorption term,  $V_{qg}$ , accumulated over time, depends also on the previously introduced quantities, and in addition, the coupling constant,

$$e^{-\frac{i}{2}V_{qg} \Delta x^+} \sim f \left[ g, \frac{2L\Delta x^+}{(2a_\perp)^2}, \frac{m_q a_\perp}{\pi}, \frac{1}{K} \right]. \quad (5)$$

The dependence on the third quantity reflects the ratio between the quark-spin-flip and nonflip transition widths, and we refer to Fig. 4 of Ref. [29] as an illustration. The fourth quantity indicates the softest gluon being emitted/absorbed.

Third, there is an effect from the medium interaction term,  $V_A$ . Here we consider a time duration  $\Delta x^+$  that is multiples of the layer thickness  $\tau$ , in order to be in the situation where one is properly sensitive to several sources that are uncorrelated in the  $x^+$  direction. The medium-interaction action depends on two dimensionless variables,

$$e^{-\frac{i}{2}V_A \Delta x^+} \sim f \left[ \frac{g^2 \tilde{\mu} a_\perp}{\sqrt{\tau}} \Delta x^+, \frac{m_q a_\perp}{\pi} \right]. \quad (6)$$

Here the combination  $g^2 \tilde{\mu} a_\perp / \sqrt{\tau}$  must appear together in this way since  $g^2$ ,  $\tilde{\mu}$ , and  $\tau$  in fact only appear in the calculation in this combination, see Eq. (A8). Taking  $\Delta x^+ \rightarrow \tau$  for one layer, and then adding together  $N_\eta$  layers of squared color charge density (added at the level of squares because the interaction is a diffusion-type process in transverse momentum), the first argument leads to the emergence of the saturation scale

$$Q_s^2 = C_F (g^2 \tilde{\mu})^2 L_\eta / (2\pi^2) \quad (7)$$

on the lattice,  $Q_s a_\perp$ . The second quantity is the ratio between the smallest and the largest transverse momentum that can be transferred by the medium.

In total, the full process combining all three terms would depend on the above-introduced quantities. We summarize those quantities and address potential constraints in setting up simulation parameters:

- (1) The *coupling constant*  $g$ , and  $g = 1$  in this work.
- (2) The *free action*  $S_{\text{free}} \equiv L_\eta \lambda_{UV}^2 / p^+$ . Since the largest transverse momentum a particle can acquire is  $\lambda_{UV}$ , we can interpret  $p^+ / \lambda_{UV}^2$  as the coherence length of quantum diffusion and gluon emission/absorption. Thus  $S_{\text{free}}$  characterizes the length scale in  $x^+$  at which the jet becomes noneikonal, cf. the noneikonal parameter defined in Refs. [53–55].
- (3) The *quark mass* in the unit of the lattice UV cutoff,  $m_q a_\perp / \pi$ . When its value is small,  $m_q a_\perp / \pi \approx 0$ , the quark-spin-flip gluon emission/absorption would be suppressed. If its value is too large, the kinetic energy term cannot resolve different transverse momentum modes.
- (4) The *saturation scale* in the unit of the lattice UV cutoff,  $Q_s a_\perp / \pi$ . It should be that  $Q_s a_\perp / \pi \ll 1$ ; otherwise, the medium momentum transfer cannot be appropriately accessed on the lattice.
- (5) The *medium IR regulator* in the unit of the lattice UV cutoff,  $m_g a_\perp / \pi$ . This “gluon mass”  $m_g$  is often introduced as the infrared screening scale of the medium, similar to the Debye mass in Gyulassy-Wang and other model potentials [56–59]. Note the mass of the dynamical gluon in the  $|qg\rangle$  sector of the Fock space is always zero. An eligible value of  $m_g$  should be covered by the momentum range on the transverse lattice  $[\lambda_{IR}, \lambda_{UV}]$ , at the same time smaller than the saturation scale  $Q_s$ . This constraint reads

$$\frac{1}{N_\perp} \ll \frac{m_g a_\perp}{\pi} \ll \frac{Q_s a_\perp}{\pi}. \quad (8)$$

The continuum limit,  $a_\perp \rightarrow 0$ , is taken by letting  $N_\perp \rightarrow \infty$  so that  $Q_s a_\perp / \pi \rightarrow 0$  while  $Q_s L_\perp / \pi$  remains constant.

- (6) The *z resolution* and cutoff,  $1/K$ . In the continuum limit,  $K \rightarrow \infty$ .

In running the numerical simulation, choosing parameters that satisfy the aforementioned conditions helps ensure that the physics of interest is captured on the discrete basis space. We refer to Appendix C of Ref. [39] for a more detailed explanation of this topic.

### III. $\hat{q}$ IN THE EIKONAL LIMIT, USING WILSON LINE CORRELATORS

In studying the phenomenon of jet momentum broadening inside a medium, a characteristic quantity to examine is the quenching parameter  $\hat{q}$  [9,60–63], defined as

$$\hat{q} = \frac{\Delta \langle p_\perp^2(x^+) \rangle}{\Delta x^+}. \quad (9)$$

It characterizes the mean square momentum transfer to the jet per unit length in the medium.

In the eikonal limit, when one can express the propagation of a parton through a medium in terms of Wilson

lines,  $\hat{q}$  can be derived analytically using the Wilson line correlators. In this section, we derive it first for a single particle state, then for a quark-gluon state.

The derivation for the single particle state has already been developed in the Wilson line formalism (e.g., Ref. [10]). The purpose of our revisiting this problem is twofold. First, we perform the derivation in the context of the formulated basis space in Sec. II, so that it could help interpret and verify in the eikonal limit the results obtained from the numerical simulations. Second, the derivation for the single particle prepares the necessary ingredients for the more complicated case of the quark-gluon state.

The existing derivations for the quark-gluon state usually use specific truncations and approximations. One considers the quark-gluon state as initially split from a single quark state. Thus the two-particle state resides in the triplet subspace. One often also takes the large  $N_c$  limit, such that some correlations can be neglected, e.g., Ref. [49]. Here, we carry out the calculation in its full color space and keep  $N_c$  finite ( $N_c = 3$ ).

### A. The single particle state

The expectation value of the transverse momentum square can be calculated directly knowing the state vector,  $\langle p_\perp^2(x^+) \rangle = \langle \psi; x^+ | \hat{p}_\perp^2 | \psi; x^+ \rangle$ . In the eikonal limit of  $p^+ = \infty$ , only the  $V_A$  term survives in the Hamiltonian, and the evolution operator reduces to the Wilson line.

For a quark, the Wilson line in the fundamental representation reads

$$U_F(0, x^+; \vec{x}_\perp) \equiv T_+ \exp\left(-ig \int_0^{x^+} dz^+ \mathcal{A}_a^-(\vec{x}_\perp, z^+) T^a\right), \quad (10)$$

in which  $T^a$  is the SU(3) generator in the fundamental representation, i.e., the Gell-Mann matrices. Replacing  $T^a$  by the generators in the adjoint representation,  $t^a$ , one gets the adjoint Wilson line for the gluon,  $U_A(0, x^+; \vec{x}_\perp)$ . The Wilson line in the above expression is a matrix in the corresponding color space.

Then, the color- $\beta$  component of the evolved state that is initially in color state  $\alpha$  reads

$$|\psi; x^+\rangle_{\text{Eik}} = \int_{\mathbf{x}} \tilde{\phi}(\vec{x}_\perp) U_F(0, x^+; \vec{x}_\perp)_{\beta\alpha} |\vec{x}_\perp\rangle, \quad (11)$$

in which the initial state is written as a wave function in the coordinate basis,  $|\psi; 0\rangle = \int_{\mathbf{x}} \tilde{\phi}(\vec{x}_\perp) |\vec{x}_\perp\rangle$  with the normalization  $\int_{\mathbf{x}} \langle \vec{x}_\perp | \vec{x}_\perp \rangle = 1$ .<sup>2</sup>

<sup>2</sup>Here and throughout the paper we use the shorthand notation  $\int_{\mathbf{p}} \equiv \int d^2 p_\perp / (2\pi)^2$  and  $\int_{\mathbf{r}} \equiv \int d^2 r_\perp$ .

In calculating  $\langle p_\perp^2(x^+) \rangle$ , the initial color space is averaged over, and the final space is summed over, therefore

$$\begin{aligned} \langle p_\perp^2(x^+) \rangle_{\text{Eik}} &= \int_{\mathbf{p}} \vec{p}_\perp^2 \int_{\mathbf{x}, \mathbf{y}} \tilde{\phi}^*(\vec{x}_\perp) \tilde{\phi}(\vec{y}_\perp) e^{-i\vec{p}_\perp \cdot (\vec{x}_\perp - \vec{y}_\perp)} \\ &\times \sum_{\beta=1}^{N_c} \frac{1}{N_c} \sum_{\alpha=1}^{N_c} \langle U_F^\dagger(0, x^+; \vec{x}_\perp)_{\alpha\beta} U_F(0, x^+; \vec{y}_\perp)_{\beta\alpha} \rangle_m. \end{aligned} \quad (12)$$

In the second line, the hermitian conjugate of the Wilson line can be viewed as the  $S$  matrix of an antiquark. Consequently, we recognize the second line of the equation as the forward scattering amplitude of an effective quark-antiquark dipole and write it as

$$\begin{aligned} S_F(0, x^+; |\vec{x}_\perp - \vec{y}_\perp|) &= \frac{1}{N_c} \text{Tr} \langle U_F^\dagger(0, x^+; \vec{x}_\perp) U_F(0, x^+; \vec{y}_\perp) \rangle_m \\ &= \exp[-C_F g^4 \hat{\mu}^2 x^+ [L(0) - L(|\vec{x}_\perp - \vec{y}_\perp|)]], \end{aligned} \quad (13)$$

in which

$$L(r = |\vec{x}_\perp - \vec{y}_\perp|) = \int_{\mathbf{k}} \frac{e^{-i\vec{k}_\perp \cdot (\vec{x}_\perp - \vec{y}_\perp)}}{(m_g^2 + \vec{k}_\perp^2)^2} = \frac{m_g r K_1(m_g r)}{4\pi m_g^2}. \quad (14)$$

The summation over the color state of the quark amounts to the effective  $\bar{q}q$  state being in the color singlet state.

Then the momentum transfer in Eq. (12) can be evaluated by taking the order derivative of the Wilson line correlator at the zero separation limit,

$$\begin{aligned} \langle p_\perp^2(x^+) \rangle_{\text{Eik}} &= \langle p_\perp^2(0) \rangle - \nabla_r^2 S_F(0, x^+; \vec{r}_\perp) |_{\vec{r}_\perp = \vec{0}_\perp}, \\ &= \langle p_\perp^2(0) \rangle + \hat{q}_{\text{Eik}} x^+. \end{aligned} \quad (15)$$

An alternative way to perform the derivation is to keep the momentum integral  $\int_{\mathbf{p}}$  and carry out the coordinate integral  $\int_{\mathbf{r}}$  instead, which we discuss in more detail in Appendix B. The quenching parameter  $\hat{q}$  as defined in Eq. (9) follows as

$$\hat{q}_{\text{Eik}} = 4\pi \hat{q}_0 \mathcal{G}_2, \quad \hat{q}_0 \equiv C_F g^4 \hat{\mu}^2 \frac{1}{4\pi}. \quad (16)$$

The ‘‘bare’’ quenching parameter  $\hat{q}_0$  is the effective speed for a quark reaching the saturation scale with half the evolution time, i.e.,  $\hat{q}_0 = Q_s^2 / 2L_\eta$ . The quantity  $\mathcal{G}_2$  contains a logarithmic divergence,

$$\begin{aligned} \mathcal{G}_2 &= -\nabla_r^2 L(r) |_{r=0}, \\ &= \frac{1}{4\pi} \left\{ \log \left[ 1 + \frac{1}{(m_g a_\perp / \pi)^2} \right] - \frac{1}{1 + (m_g a_\perp / \pi)^2} \right\}. \end{aligned} \quad (17)$$

In analogy, one gets the  $\hat{q}$  for a gluon state replacing  $C_F = (N_c^2 - 1)/(2N_c)$  by  $C_A = N_c$  in Eq. (16).

In the above derivation, we do not take into account the effect from the momentum space lattice edges, allowing transverse momentum square increase linearly over time boundlessly. However, on the finite lattice, there is an asymptotic value for  $\langle p_\perp^2 \rangle$ . This happens when the particles are distributed uniformly in the whole momentum space,

$$\langle p_\perp^2 \rangle_{\text{asy}} = \frac{1}{(2N_\perp)^2} \sum_{i=-N_\perp}^{N_\perp-1} \sum_{j=-N_\perp}^{N_\perp-1} (i^2 + j^2) \left( \frac{\pi}{L_\perp} \right)^2 \approx \frac{2}{3} \left( \frac{\pi}{a_\perp} \right)^2, \quad (18)$$

where the approximated value is obtained by taking the continuum limit.<sup>3</sup> Thus the linear growth of the momentum broadening with  $x^+$  will saturate when approaching this limit.

### B. The quark-gluon state

For a quark-gluon state, the expectation value of its total momentum squared can be evaluated from its wave function, in analogy to that of a single particle state in Eq. (12),

$$\begin{aligned} \langle p_\perp^2(x^+) \rangle_{qg,c;\text{Eik}} &= \int_{\mathbf{p}_q} \int_{\mathbf{p}_g} (\vec{p}_{q,\perp} + \vec{p}_{g,\perp})^2 \\ &\times \int_{\mathbf{x}_q} \int_{\mathbf{y}_q} \int_{\mathbf{x}_g} \int_{\mathbf{y}_g} \tilde{\phi}^*(\vec{x}_{q,\perp}, \vec{x}_{g,\perp}) \tilde{\phi}(\vec{y}_{q,\perp}, \vec{y}_{g,\perp}) \\ &\times e^{-i\vec{p}_{q,\perp} \cdot (\vec{x}_{q,\perp} - \vec{y}_{q,\perp})} e^{-i\vec{p}_{g,\perp} \cdot (\vec{x}_{g,\perp} - \vec{y}_{g,\perp})} \\ &\times \mathcal{P}_{qg,c}(0, x^+; \vec{x}_{q,\perp}, \vec{x}_{g,\perp}, \vec{y}_{q,\perp}, \vec{y}_{g,\perp}). \end{aligned} \quad (20)$$

Here the initial state is written in form of the wave function in the coordinate basis,  $|\psi; 0\rangle = \int_{\mathbf{x}_q} \int_{\mathbf{x}_g} \tilde{\phi}(\vec{x}_{q,\perp}, \vec{x}_{g,\perp}) \times |\vec{x}_{q,\perp}, \vec{x}_{g,\perp}\rangle$ .

In the discussion for the single quark (or gluon),  $\langle p_\perp^2(x^+) \rangle$  is evaluated in the entirety of the corresponding color space, which is irreducible by itself. For a quark-gluon state, we examine the momentum broadening in each of its invariant color subspaces as well as the full. The invariant color space is indicated by the subscript ‘‘c’’ in the expression. An extensive discussion on the quark-gluon color space can be found in Appendix C. To calculate the

<sup>3</sup>In the continuum limit, this asymptotic value is evaluated by integration instead of summation,

$$\langle p_\perp^2 \rangle_{\text{asy}} = \frac{\int_{-\lambda_{UV}}^{\lambda_{UV}} dk^x \int_{-\lambda_{UV}}^{\lambda_{UV}} dk^y [(k^x)^2 + (k^y)^2]}{\int_{-\lambda_{UV}}^{\lambda_{UV}} dk^x \int_{-\lambda_{UV}}^{\lambda_{UV}} dk^y} = \frac{2}{3} \lambda_{UV}^2, \quad (19)$$

then on the lattice  $\lambda_{UV} = \pi/a_\perp$ .

probability, one must square the wave function, keeping the colors of the incoming particles the same in the amplitude and the conjugate amplitude, and summing over the outgoing color in the full color space. The probability function of a quark-gluon state in the color state  $c$  is written as  $\mathcal{P}_{qg,c}$ ,

$$\mathcal{P}_{qg,c} \equiv \sum_{i=1}^{N_c} \sum_{a=1}^{d_A} \langle \psi_{\bar{q}\bar{g}qg, \{i,a,i,a\}} | \mathcal{S}_{\bar{q}\bar{g}} | \psi_{\bar{q}\bar{g}qg, \bar{c}(\bar{q}\bar{g})c(qg)} \rangle, \quad (21)$$

in which

$$\begin{aligned} \mathcal{S}_{\bar{q}\bar{g}qg}(0, x^+; \vec{x}_{q,\perp}, \vec{x}_{g,\perp}, \vec{y}_{q,\perp}, \vec{y}_{g,\perp}) \\ = \langle U_F^\dagger(\vec{x}_{q,\perp}) \otimes U_A^\dagger(\vec{x}_{g,\perp}) \otimes U_F(\vec{y}_{q,\perp}) \otimes U_A(\vec{y}_{g,\perp}) \rangle_m \end{aligned} \quad (22)$$

is the  $\bar{q}\bar{g}qg$  four-point Wilson line correlator. Similarly to the  $q$  state, the summation over the color states of the  $qg$  state amounts to the effective  $\bar{q}\bar{g}qg$  state being color singlets. We leave out the time argument in the Wilson lines for simplicity in the above expression. The details of  $\mathcal{S}_{\bar{q}\bar{g}qg}$  and  $\mathcal{P}_{qg,c}$  can be found in Appendix D, see also Ref. [64] for a study and analysis of  $\mathcal{S}_{\bar{q}\bar{g}qg}$ . Note that in spite of the bracket notation in Eq. (22), for our purpose this color structure is already at the probability level, with the  $\bar{q}\bar{g}$  corresponding to a quark (gluon) in the conjugate wave function.

The quark-gluon momentum squared in Eq. (20) can be split into three terms:

$$\begin{aligned} \langle p_\perp^2(x^+) \rangle_{qg,c;\text{Eik}} &= \langle \vec{p}_{q,\perp}^2(x^+) \rangle_{\text{Eik}} + \langle \vec{p}_{g,\perp}^2(x^+) \rangle_{\text{Eik}} \\ &+ 2\langle \vec{p}_{q,\perp}(x^+) \cdot \vec{p}_{g,\perp}(x^+) \rangle_{c;\text{Eik}}. \end{aligned} \quad (23)$$

The first two terms turn out to be the same as Eq. (15) with the corresponding Casimir. For the third term, it is more convenient to change to relative and center-of-mass coordinates

$$\begin{aligned} \vec{v}_\perp &= \vec{x}_{q,\perp} - \vec{x}_{g,\perp}, & \vec{R}_\perp &= z\vec{x}_{q,\perp} + (1-z)\vec{y}_{g,\perp}, \\ \vec{u}_{q,\perp} &= \vec{x}_{q,\perp} - \vec{y}_{q,\perp}, & \vec{u}_{g,\perp} &= \vec{x}_{g,\perp} - \vec{y}_{g,\perp}, \end{aligned} \quad (24)$$

which allows us to express the momentum correlation as

$$\begin{aligned} \langle \vec{p}_{q,\perp}(x^+) \cdot \vec{p}_{g,\perp}(x^+) \rangle_{c;\text{Eik}} \\ = \int_{\mathbf{v}} f_{\text{Rel}}(\vec{v}_\perp) \vec{\nabla}_{u,q} \cdot \vec{\nabla}_{u,g} \\ \times \mathcal{P}_{qg,c}(0, x^+; \vec{v}_\perp + \vec{u}_{q,\perp}, \vec{u}_{q,\perp}, \vec{v}_\perp, \vec{u}_{g,\perp} - \vec{u}_{g,\perp}) \Big|_{\vec{u}_{q,\perp}, \vec{u}_{g,\perp} = \vec{0}_\perp}. \end{aligned} \quad (25)$$

Note that we take advantage of the Wilson line correlator being translationally invariant in the above expression;

see Eq. (D12) and discussions for detail. The quantity  $f_{\text{Rel}}(\vec{v}_\perp)$  is the distribution function of the quark-gluon relative coordinate  $\vec{v}_\perp$ , and it can be obtained by integrating the wave function square over the center-of-mass coordinate  $\vec{R}_\perp$ ,

$$f_{\text{Rel}}(\vec{v}_\perp) \equiv \int_{\mathbf{R}} |\tilde{\phi}(\vec{x}_{g,\perp}, \vec{x}_{q,\perp})|^2. \quad (26)$$

We find that the cross term depends on the initial color configuration of the quark-gluon state and the separation between the quark and the gluon,

$$\langle \vec{p}_{q,\perp}(x^+) \cdot \vec{p}_{g,\perp}(x^+) \rangle_{c;\text{Eik}} = \begin{cases} 0, & c = 3 \otimes 8 \\ -\frac{N_c \sqrt{2}}{2} f_{12}, & c = 3 \\ -\frac{\sqrt{2}}{2} f_{12}, & c = \bar{6} \\ \frac{\sqrt{2}}{2} f_{12}, & c = 15 \end{cases}, \quad (27)$$

in which  $f_{12} = -\int_{\mathbf{v}} f_{\text{Rel}}(\vec{v}_\perp) s_{12}(v_\perp)$  and the explicit form of the function  $s_{12}$  is given in Eq. (D29) in the Appendix. We leave the details of the derivation to Appendix C 2. From Eq. (27), one can see that if the quark and the gluon are in a color-uncorrelated state, as is effectively the case if one sums over the whole  $3 \otimes 8$ -dimensional color space of the final state, then the cross term vanishes.<sup>4</sup> For a color-correlated quark-gluon state, the cross term is large if the separation between the two particles,  $v$  is small, and becomes negligible when the separation set by the wave function  $\tilde{\phi}$  gets large,  $v > 1/m_g$ . In particular, if the quark-gluon state is a single momentum state, it is maximally delocalized, and the relative coordinate distribution is uniform,  $f_{\text{Rel}}(\vec{v}_\perp) = 1/(2L_\perp)^2$ , leading to a very weak correlation between the quark and gluon.

## IV. $\hat{q}$ IN THE NONEIKONAL REGIME, USING NUMERICAL SIMULATIONS

### A. The single quark state $|q\rangle$

We first perform the simulations in the leading Fock sector of  $|q\rangle$ , and study the evolution of the quark's transverse momentum. In the eikonal limit of  $p^+ = \infty$ , the quark's transverse momentum square  $\langle p_\perp^2(x^+) \rangle$  is expected to grow linearly over the evolution time  $x^+$ , as we have obtained from Eq. (15) in Sec. III A. We verify our numerical calculations in the eikonal limit by comparing them to the analytical expectation and also go beyond this

<sup>4</sup>Note that if one sums the coefficients of the representations 3,  $\bar{6}$ , and 15 in Eq. (27) weighted by the dimension of the representation, one gets zero; see Eq. (D19) and discussions around it.

limit by letting the quark have finite  $p^+$ . We then study the dependence on the medium IR regulator  $m_g a_\perp/\pi$  and the saturation scale  $Q_s a_\perp/\pi$ . Note that though the quark mass enters the kinetic energy term, as in Eq. (4), it acts as an overall phase factor in calculating  $\langle p_\perp^2(x^+) \rangle$  and therefore does not contribute.

### 1. Dependence on $p^+$

The longitudinal momentum  $p^+$  signifies how fast the quark jet travels through the medium, and its effect is related to the structure of the medium along  $x^+$ . The medium, according to the MV model, should be singularly uncorrelated as  $\langle \mathcal{A}(x^+) \mathcal{A}(y^+) \rangle_m \propto \delta(x^+ - y^+)$  as in Eq. (2). On the amplitude level, it means that  $\mathcal{A}(x^+)$  is stochastic, which is realized numerically with a  $x^+$  resolution of  $\tau$ ; this is in analogy to having an  $x_\perp$  resolution of  $a_\perp$  in the transverse dimension, see also Eq. (A8). Consequently, to match the analytical formulation, one should take the continuous limit of  $a_\perp \rightarrow 0$  ( $N_\perp \rightarrow \infty$  while fixing  $L_\perp$ ) and  $\tau \rightarrow 0$  ( $N_\eta \rightarrow \infty$  while fixing  $L_\eta$ ). However, in reality, the medium, as a composition of quarks and gluons, is more likely to have a finite correlation length. In the transverse dimension, the medium IR regulator  $m_g$  plays such a role of screening. Considering the medium in its rest frame and assuming that it is isotropic, this would imply that the duration of each layer would be of the same magnitude, such that  $\tau \sim 1/m_g$ . When the medium is longitudinally boosted, e.g., in a frame with its  $p^- \approx \infty$ , both  $\tau$  and  $L_\eta$  get contracted, but  $N_\eta$  will stay the same as in the medium rest frame. Thus, to study a finite energy jet it is interesting to also perform simulations with a finite  $\tau$ .

To proceed, we first study the dependence of the momentum broadening on  $N_\eta$ . In Fig. 1, we present  $\langle p_\perp^2(x^+) \rangle$  and the extracted values of the quenching parameter  $\hat{q}$  [calculated according to Eq. (9), with  $\Delta x^+ = L_\eta$ ] at various  $N_\eta$  while fixing  $L_\eta$ . The value at each data point is averaged over 10 configurations, and the band width is the standard deviation indicating the uncertainties from the configuration fluctuation. Though in both infinite and finite  $p^+$  cases, the simulation results converge to the analytical expectation as  $N_\eta$  increases, the latter happens at a slower pace. We have three key observations. First, in the continuous limit of  $N_\eta \rightarrow \infty$ , the kinetic energy term does not affect the momentum broadening and the value of  $\hat{q}$ . Thus the analytical result derived in the eikonal limit in Sec. III A also applies to finite  $p^+$  cases; see also Ref. [65]. Second, the convergence to the eikonal analytical result as  $N_\eta \rightarrow \infty$  is slower at a larger saturation scale, as shown by the comparison between Figs. 1(a) and 1(b). Third, at a finite  $N_\eta$ , in particular when  $\tau = 1/m_g$ , a finite  $p^+$  leads to a decrease in  $\hat{q}$ .

It is also interesting to observe the momentum evolution within a layer. The results at  $N_\eta = 4$  in Fig. 1 exemplify

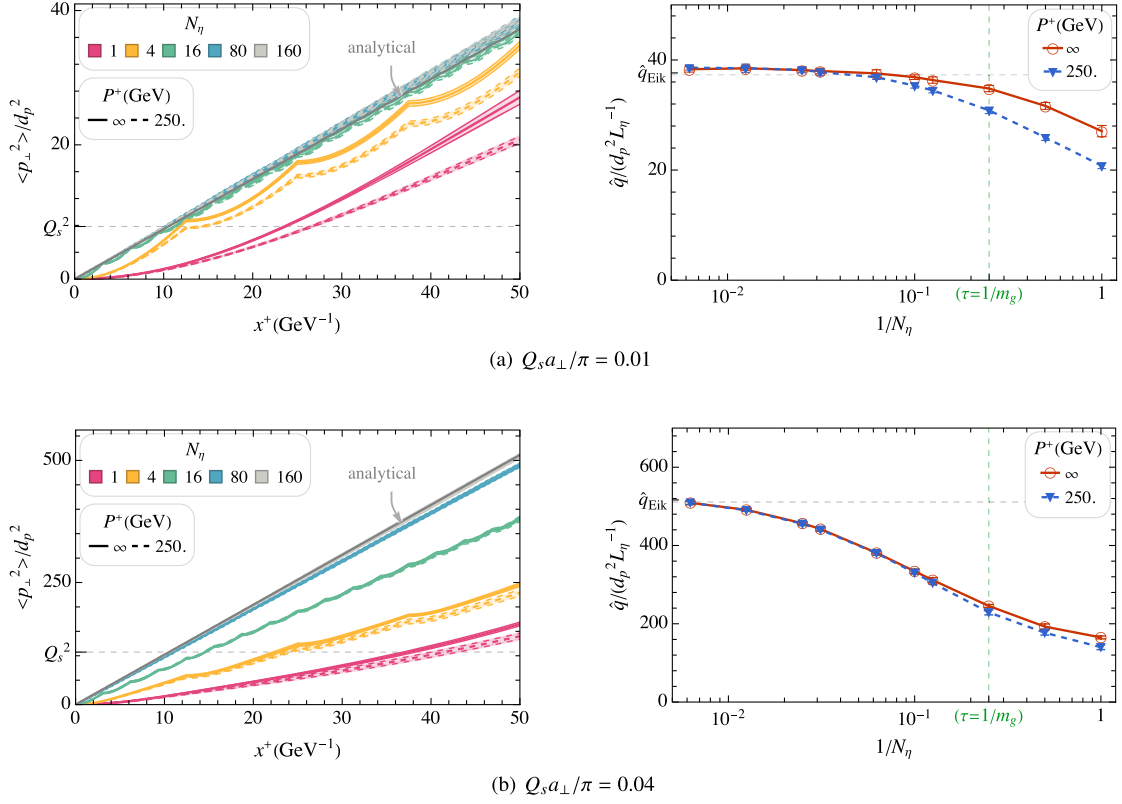


FIG. 1. The dependence of the momentum broadening on the number of medium layers  $N_\eta$ , at (a) a smaller and (b) a larger saturation scale  $Q_s$ . Left panels: the transverse momentum square  $\langle p_\perp^2(x^+) \rangle$  as a function of  $x^+$  at various  $N_\eta$  with fixed  $m_g a_\perp / \pi = 0.005$  and  $Q_s$  [with the bare  $Q_s^2 / d_p^2$  given by Eq. (7) indicated by the horizontal dashed line]. Results at infinite (finite)  $p^+$  are shown in solid (dashed) lines, and the band indicates the fluctuation from 10 configurations. Right panels: the quenching parameter  $\hat{q}$  as a function of  $1/N_\eta$ . The green vertical dashed line indicates the value of  $1/N_\eta$  at which  $\tau = 1/m_g$ . The eikonal analytical results according to Eq. (15) are in the solid black line indicated as “analytical” in the left panels, and in the dashed gray line indicated as “ $\hat{q}_{\text{Eik}}$ ” in the right panels.

that  $\langle p_\perp^2(x^+) \rangle$  grows quadratically within a layer while linearly across layers. The analytical derivation in Sec. III A inherits the treatment of  $\langle \rho(x^+) \rho(y^+) \rangle_m \propto \delta(x^+ - y^+)$  from the MV model, therefore only accounts for the behavior across layers. To understand the evolution within a layer analytically, let us calculate the Wilson line in such a scenario, there the  $x^+$  integral becomes

$$\int_0^{\delta x^+} dx^+ \int_0^{\delta x^+} dy^+ \langle \rho_a(x^+, \vec{x}_\perp) \rho_b(y^+, \vec{y}_\perp) \rangle_m = \delta_{ab} \delta^2(\vec{x}_\perp - \vec{y}_\perp) g^2 \tilde{\mu}^2 \begin{cases} \delta x^+, & \delta x^+ \geq \tau \\ (\delta x^+)^2 / \tau, & \delta x^+ < \tau \end{cases} \quad (28)$$

The resulting Wilson line within a layer, i.e.,  $\delta x^+ < \tau$ , is thus  $S_F(0, \delta x^+; r) = e^{-C_F g^4 \tilde{\mu}^2 (\delta x^+)^2 / \tau [L(0) - L(r)]}$ , in comparison to Eq. (13) for the Wilson line across multiple layers. The observation from the numerical simulation verifies this quadratic/linear behavior of the squared momentum.

For a closer examination, we present the transverse momentum distribution  $f(p_\perp)$  at both infinite and finite

$p^+$  in Fig. 2. Note that the phase space of states on the discrete square lattice is different from that in the continuous case, and their ratio is indicated by the dashed gray line in the left panel. More information can be found in Appendix A 1. We can see that the typical transverse momentum is of order  $\sqrt{\hat{q} L_\eta}$ , but there is a long power law tail up to higher  $p_\perp$ . The difference between different values of  $N_\eta$  is smooth as a function of  $p_\perp$ , but the lower typical  $p_\perp$  for finite  $P^+$  at small  $N_\eta$  is caused by a depletion of the highest  $p_\perp$  modes.

Next, we take the estimation of  $\tau = 1/m_g$  such that  $N_\eta = 4$  with  $L_\eta = 50 \text{ GeV}^{-1}$ , and study the  $p^+$  dependence. Note that both  $N_\eta$  and  $L_\eta / p^+$  are boost invariant, and here we fix  $L_\eta$  and  $\tau$ . One could alternatively fix  $p^+$  and  $N_\eta$  but vary  $L_\eta$  (and thus  $\tau$ ) to obtain the same results. The results are shown in Fig. 3(a), and the results with  $N_\eta = 8$  are in Fig. 3(b) for comparison. We find that with a finite number of layers, a smaller  $p^+$  leads to a smaller  $\hat{q}$ . Then towards the eikonal limit of  $p^+ = \infty$ , the obtained  $\hat{q}$  gets closer to the analytical result calculated with an infinite number of layers. But even at  $\tau / p^+ = 0$ , i.e., in the eikonal



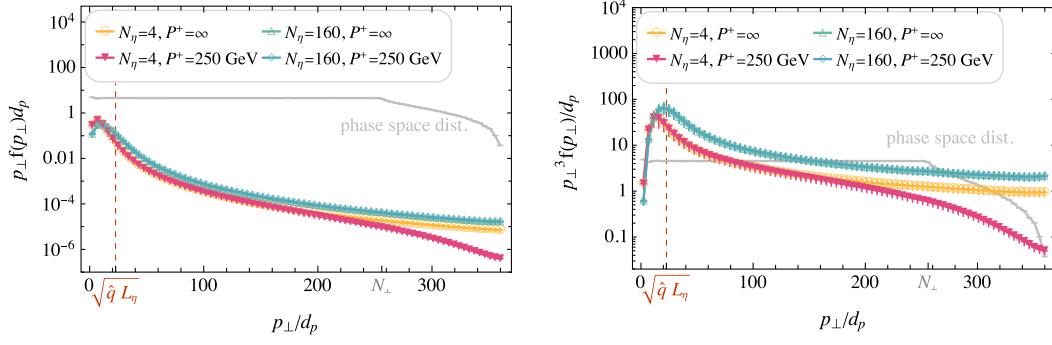


FIG. 2. The transverse momentum distribution  $p_{\perp} f(p_{\perp}) d_p$  in the left panel and  $p_{\perp}^3 f(p_{\perp})/d_p$  in the right panel, both as a function of  $p_{\perp}$  at infinite and finite  $p^+$ . The light gray line indicates the relative size of the basis state phase space to the continuous case, according to  $R(p_{\perp})$  in Eq. (A6).

case, the obtained  $\hat{q}$  does not always agree with the analytical ones, especially at larger  $Q_s$ . This difference results from  $N_{\eta}$  being finite in the setup. As we have seen earlier in Fig. 1, a larger  $Q_s$  requires a larger value of  $N_{\eta}$  to restore the analytical results. In addition, the results obtained at different  $L_{\eta}$  overlap, showing that  $\hat{q}$  in the units of  $d_p^2 L_{\eta}^{-1}$  only depends on the boost-invariant quantity of  $\tau/p^+$ , but not  $p^+$  or  $L_{\eta}$  separately.

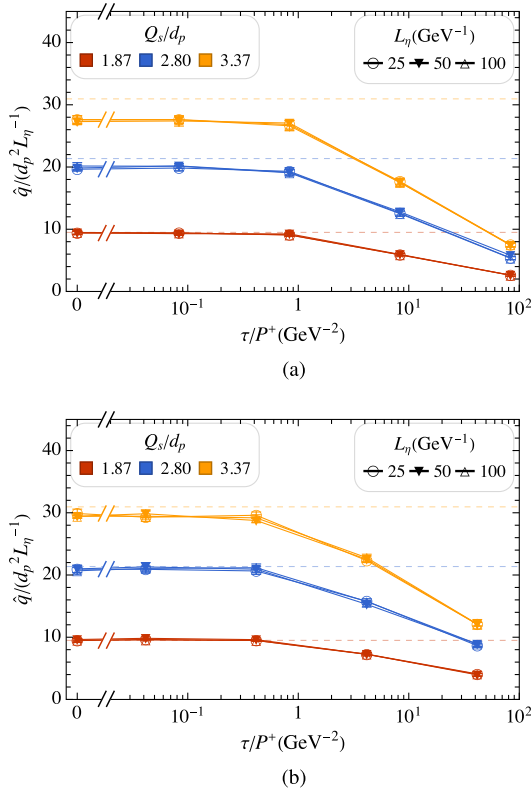


FIG. 3. The dependence of  $\hat{q}$  on the particle longitudinal momentum  $p^+$  at various saturation scale  $Q_s$  and at a fixed  $m_g a_{\perp}/\pi = 0.04$ , with (a)  $N_{\eta} = 4$  and (b)  $N_{\eta} = 8$ . The results at different  $L_{\eta}$  overlap with each other. The horizontal lines are the values of  $\hat{q}_{\text{Eik}}$  at  $\tau/p^+ = 0$  according to Eq. (15).

## 2. Dependence on $m_g a_{\perp}/\pi$

The quenching parameter  $\hat{q}$  is expected to have a logarithmic dependence on  $m_g a_{\perp}/\pi$  according to the analysis in Sec. III A. In the numerical simulations, one can separately change one or multiple of the three quantities  $L_{\perp}$ ,  $N_{\perp}$ , and  $m_g$ , but the physical results should remain the same if  $m_g a_{\perp}/\pi$  are fixed. Yet there is a prerequisite, the medium IR regulator  $m_g$  should be covered by the lattice resolution, i.e.,  $m_g d_p (= m_g L_{\perp}/\pi) > 1$ ; otherwise, the lattice IR cutoff  $d_p$  would effectively act as the IR regulator instead.

As shown in Fig. 4, the results obtained at  $m_g d_p > 1$  agree with the analytical results at each  $m_g a_{\perp}/\pi$ , whereas that at  $m_g d_p < 1$  deviates below since the screening mass in the medium is no longer sufficiently represented by  $m_g$ . One could also see that the quenching parameter relative to its bare value,  $\hat{q}/\hat{q}_0$ , depends logarithmically on  $m_g a_{\perp}/\pi$ , but not on  $Q_s/d_p$ .

## 3. Dependence on the saturation scale $Q_s$

The quenching parameter  $\hat{q}$  is expected to have a linear dependence on  $Q_s$  defined by (7), according to the analysis in Sec. III A. We show in Fig. 5 that the transverse momentum squared  $\langle p_{\perp}^2(x^+) \rangle$  as a function of  $x^+$  at various  $Q_s/d_p$  agrees with the analytical expectation. Keeping  $m_g a_{\perp}/\pi$  fixed, one could also see that  $\hat{q}$  grows linearly with  $Q_s^2/d_p^2$ .

## B. The quark-gluon state $|qg\rangle$

Having studied the momentum broadening of a single particle state, we now proceed to the two-particle state  $|qg\rangle$ . When traversing through the medium, the quark and the gluon each exchange color and transverse momentum with the medium, in the manner of a single particle. Meanwhile, the correlation between them introduces additional complexity in examining their total and relative momenta. The quark-gluon correlation is characterized by their separation

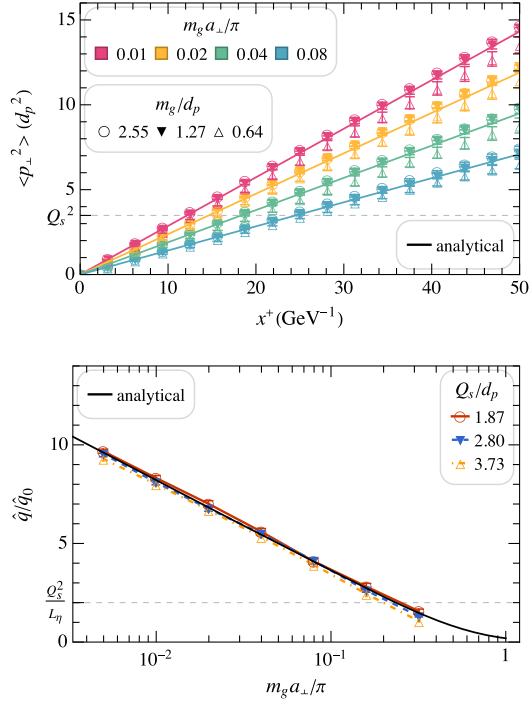


FIG. 4. The dependence on  $m_g a_{\perp} / \pi$  of the momentum broadening. Top panel: the transverse momentum square  $\langle p_{\perp}^2(x^+) \rangle$  as a function of  $x^+$  at various  $m_g a_{\perp} / \pi$  and a fixed  $Q_s$  [with the bare  $Q_s^2 / d_p^2$  given by Eq. (7) indicated by the horizontal dashed line]. The data at the two larger  $m_g d_p > 1$ , in open circles and solid triangles, overlap with each other, whereas that at the smaller  $m_g d_p < 1$ , in the open triangle, deviates below the former. Bottom panel: the quenching parameter  $\hat{q}$  as a function of  $m_g a_{\perp} / \pi$  at various  $Q_s / d_p$  with  $m_g d_p = 1.27$ . The analytical results in the solid lines are given by Eq. (15).

in the transverse coordinate space and their color configuration, as we have studied analytically in Sec. III B. The effect of such a correlation throughout the evolution is of our interest. To this purpose, we perform the simulations with quark-gluon states in different color-correlated configurations and separated by small and large distances.

Note that in a quantum formalism, as in this work, it is impossible to assign a particle state with a specific momentum and coordinate simultaneously, which one could do easily in a classical picture. Instead, the wave function in momentum space and that in coordinate space are related by the Fourier transform. Specifically, a single coordinate state is uniformly distributed in the momentum space. Consequently, a quark-gluon state with both particles in the same coordinate mode, which one would instinctively think of as the most correlated state, is not helpful in observing momentum broadening since all  $p_{\perp}$  modes are already equally occupied before entering the medium. A more realistic and appropriate setup is to have the quark and the gluon as two Gaussian wave packets, which we adopt in the following study. The quark (gluon) is

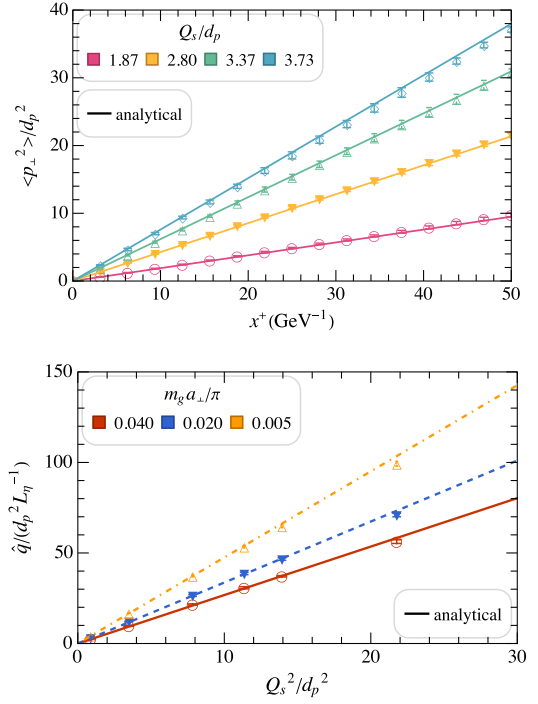


FIG. 5. The dependence on  $Q_s / d_p$  of the momentum broadening. Top panel: the transverse momentum square  $\langle p_{\perp}^2(x^+) \rangle$  as a function of  $x^+$  at various  $Q_s / d_p$  with a fixed  $m_g a_{\perp} / \pi = .04$ . Bottom panel: the quenching parameter  $\hat{q}$  as a function of  $Q_s^2 / d_p^2$  at various  $m_g a_{\perp} / \pi$ . The analytical results in the solid lines are given by Eq. (15).

centered at  $\vec{s}_{q,\perp}$  ( $\vec{s}_{g,\perp}$ ) with a width of  $w_q$  ( $w_g$ ), such that the wave function reads

$$\tilde{\phi}(\vec{r}_{q,\perp}, \vec{r}_{g,\perp}) = C e^{-\frac{1}{2} \left( \frac{\vec{r}_{q,\perp} - \vec{s}_{q,\perp}}{w_q} \right)^2} \otimes e^{-\frac{1}{2} \left( \frac{\vec{r}_{g,\perp} - \vec{s}_{g,\perp}}{w_g} \right)^2}. \quad (29)$$

Here,  $C$  is a constant determined by the normalization condition. In order to have the quark and the gluon each localized in transverse coordinate space, their Gaussian width  $w_q$  and  $w_g$  should be smaller than the inverse of their respective transferred momentum,

$$w_q, w_g < \frac{1}{\sqrt{\hat{q}_{\text{Eik}} L_{\eta}}}. \quad (30)$$

We set the initial state as given in Eqs. (29) and (30) in two cases: (a)  $\vec{s}_{q,\perp} / a_{\perp} = \vec{s}_{g,\perp} / a_{\perp} = \{0, 0\}$ , and (b)  $\vec{s}_{q,\perp} / a_{\perp} = \{0, 0\}$  and  $\vec{s}_{g,\perp} / a_{\perp} = \{0, 10\}$ ; for both cases,  $w_q = w_g = a_{\perp}$ . Figure 6 shows the distributions of the quark and the gluon in the transverse coordinate space in both cases. Note that the parameter in (b) is not special but just one choice that guarantees a large quark-gluon separation, where a separation of 10 lattice units is considerably large on a periodic 32 by 32 lattice. The distribution function of the relative transverse coordinate is

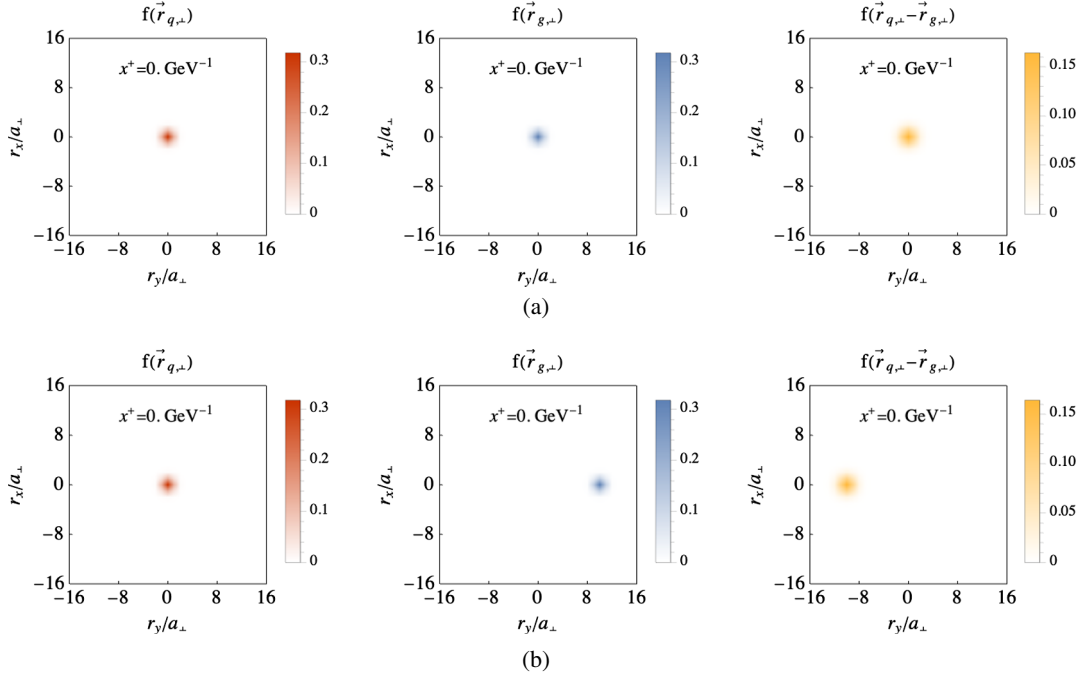


FIG. 6. Initial distributions of the quarks, the gluons, and their relative transverse coordinate for (a) a small-separation, and (b) a large-separation quark-gluon state, with  $a_{\perp} \approx 0.6$  fm.

defined as in Eq. (26), by integrating over the center-of-mass part. The single particle distribution function could also be calculated from the wave function, by integrating over the dependence on the coordinate of the other particle,

$$\begin{aligned} f_q(\vec{r}_{q,\perp}) &\equiv \int_{\vec{r}_g} |\tilde{\phi}(\vec{r}_{q,\perp}, \vec{r}_{g,\perp})|^2, \\ f_g(\vec{r}_{g,\perp}) &\equiv \int_{\vec{r}_q} |\tilde{\phi}(\vec{r}_{q,\perp}, \vec{r}_{g,\perp})|^2. \end{aligned} \quad (31)$$

### 1. Small-separation quark-gluon state

First, we study a scenario where the two particles are extensively correlated in space. We set the initial state as

given in Eqs. (29) and (30) with  $\vec{s}_{q,\perp}/a_{\perp} = \vec{s}_{g,\perp}/a_{\perp} = \{0, 0\}$  and  $w_q = w_g = a_{\perp}$ , i.e., case (a) in Fig. 6. We study the correlation by examining the evolution of  $\langle p_{\perp}^2 \rangle$  for the two-particle state.

In the eikonal limit of  $p^+ = \infty$ , the value of  $\langle p_{\perp}^2(x^+) \rangle$  can be calculated exactly according to Eq. (27). The results from numerical simulation agree with such expectations, as shown in Fig. 7. To see the momentum that gets broadened, we present the change  $\Delta \langle p_{\perp}^2 \rangle \equiv \langle p_{\perp}^2(x^+ = L_{\eta}) \rangle - \langle p_{\perp}^2(x^+ = 0) \rangle$  in these plots. The momentum broadening of the quark (gluon) individually is the same, regardless of the quark-gluon color configurations. This is because the individual particle's momentum broadening in the  $|qg\rangle$  state is the same as that of the

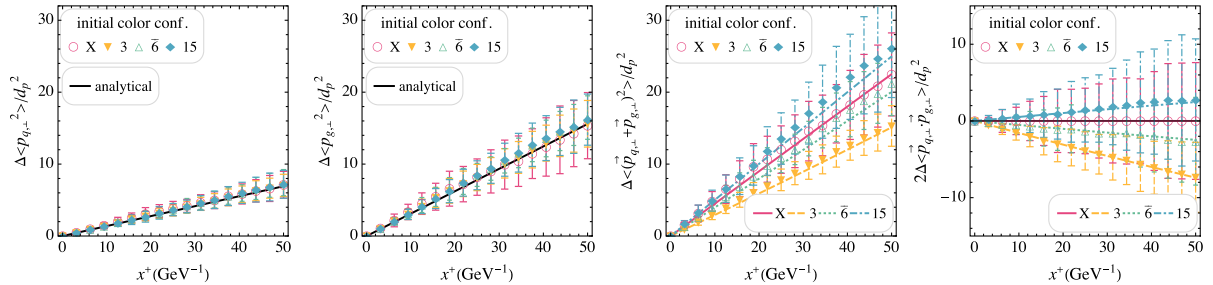


FIG. 7. The transverse momentum evolution of a small-separation quark-gluon state [distribution as shown in Fig. 6(a)] in the eikonal limit of  $p^+ = \infty$ , at  $Q_s a_{\perp} / \pi = 0.12$ . Simulation parameters:  $N_{\perp} = 16$ ,  $L_{\perp} = 50$  GeV $^{-1}$ , and  $\tau = 10$  GeV $^{-1}$ . From left to right, it shows the  $\langle p_{\perp}^2 \rangle$  of the quark, the gluon, the total, and the cross terms  $2\langle (\vec{p}_{q,\perp} \cdot \vec{p}_{g,\perp})^2 \rangle$ . The legends of open markers indicate the initial color configurations of the quark-gluon state, “X” as uncorrelated, “3” as in the triplet, “ $\bar{6}$ ” as in the antisextet, and “15” as in the deciquintuplet. The numerical values are averaged over 64 configurations, and the uncertainty bars indicate the standard deviation. The lines are analytical expectations at  $p^+ = \infty$  evaluated according to Eqs. (23) and (27).

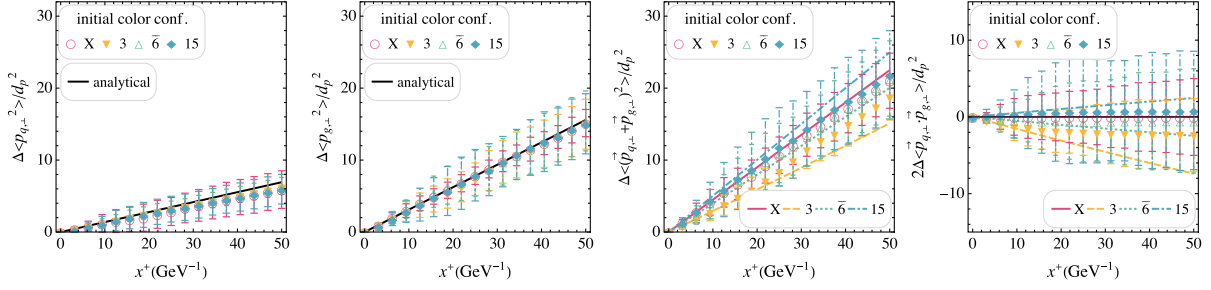


FIG. 8. The transverse momentum evolution of a small-separation quark-gluon state [distribution as shown in Fig. 6(a)] at  $p^+ = 1.5$  GeV ( $p_q^+ = 0.5$  GeV and  $p_g^+ = 1.0$  GeV) with  $m_q = 0.15$  GeV. See simulation parameters and explanation of legends and data points in the caption of Fig. 7. The lines are analytical expectations at  $p^+ = \infty$  evaluated according to Eqs. (23) and (27).

single particle. On the contrary, the total momentum differs for different color configurations. This can be understood in an intuitive way. Let us first think of the quark and the gluon coinciding in the transverse coordinate space. Then its momentum broadening would behave as a single particle state, and depends on its color configuration. Though in the simulated state, the quark and the gluon do not coincide exactly, their separation is small relative to the reaction scale of the medium; one could, therefore, still observe the difference.

Things are more complicated at a finite  $p^+$ . First, we know from the previous section that the single particle momentum broadening would be different from the eikonal case given a finite  $N_\eta$ . Second, the transverse coordinate distribution would no longer stay the same as it is initially. The quark-gluon state would spread

out, and so does its relative distribution  $f_{\text{Rel}}(\vec{v}_\perp)$ . This means that the spatial correlation between the quark and the gluon would decrease over time. The transverse coordinate distribution of the evolved state can be found in Fig. 9(a). As a result, the cross term,  $\langle \vec{p}_{q,\perp}(x^+) \cdot \vec{p}_{g,\perp}(x^+) \rangle$  would get smaller than the eikonal expectation. Figure 8 shows the results, which agree with this expectation. The differences of the total momenta among different color configurations decrease over time, as compared to the eikonal case.

Figure 10 presents the transverse momentum distribution  $p_\perp f(p_\perp) d p_\perp$  of the quark-gluon state in both the infinite and finite  $p^+$  cases. The total (relative) transverse momentum is defined as  $\vec{p}_{q,\perp} \pm \vec{p}_{g,\perp}$ . There is a difference between the total and the relative  $p_\perp$  distributions, which, while small, implies a nonzero quark-gluon correlation.

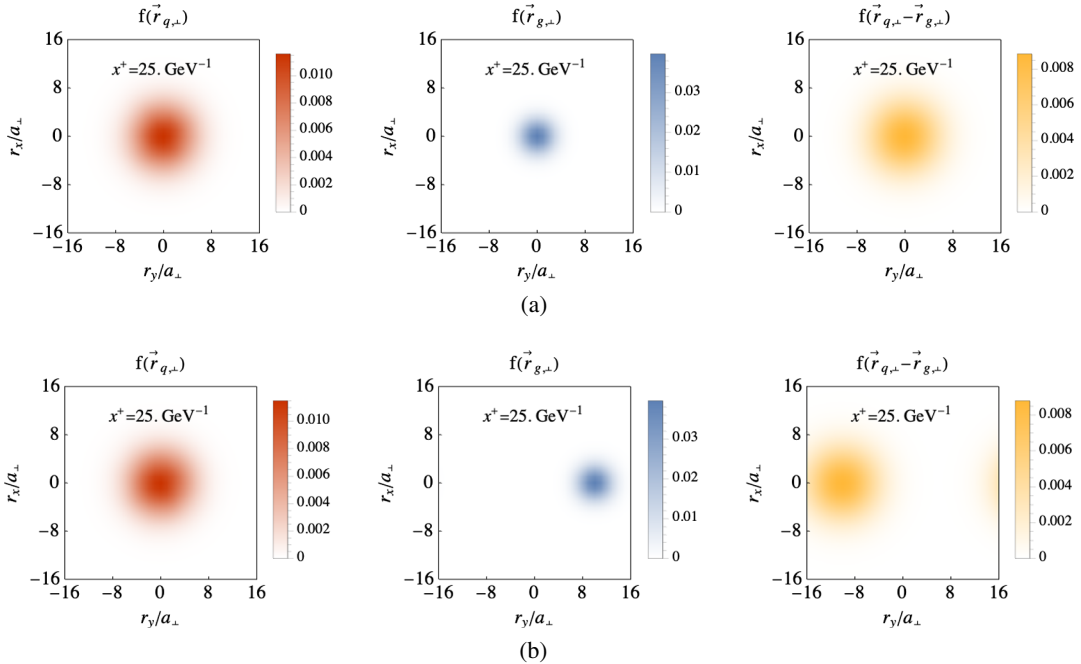


FIG. 9. Distributions of the quark's, the gluon's, and their relative transverse coordinate at a later time with  $p^+ = 1.5$  GeV. The initial state distribution of (a) is shown in Fig. 6(a), and that of (b) in Fig. 6(b).

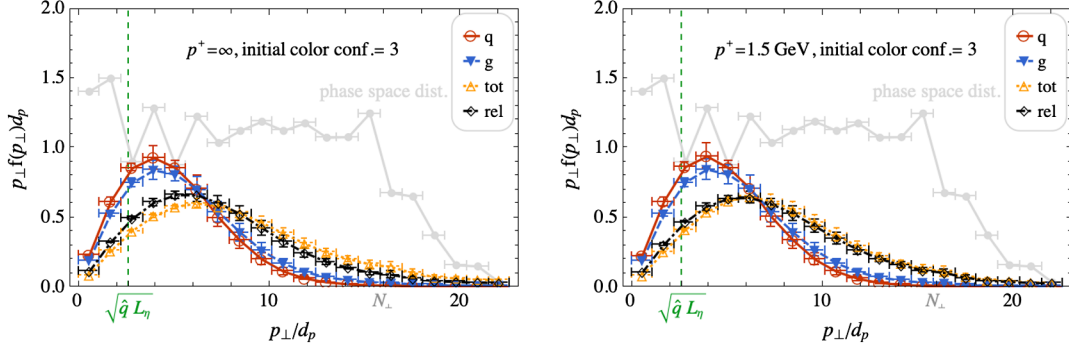


FIG. 10. The transverse momentum distribution  $p_{\perp} f(p_{\perp}) d p_{\perp}$  of the small-separation color-triplet quark-gluon state at infinite and finite  $p^+$ , after the evolution through the medium, at  $x^+ = 50 \text{ GeV}^{-1}$ . The legends “q,” “g,” “tot,” and “rel” indicate the distribution function for the quark, the gluon, their total, and their relative transverse momentum, respectively. The light gray line indicates the relative size of the basis state phase space to the continuous case, according to  $R(p_{\perp})$  in Eq. (A6).

## 2. Large-separation quark-gluon state

We then move to a scenario where the two particles are not much correlated in space. We set the initial state as given in Eqs. (29) and (30) with  $\vec{s}_{q,\perp}/a_{\perp} = \{0, 0\}$  and  $\vec{s}_{g,\perp}/a_{\perp} = \{0, 10\}$ ,  $w_q = w_g = a_{\perp}$ , i.e., case (b) in Fig. 6. We again study the correlation by examining the evolution of  $\langle p_{\perp}^2 \rangle$  for the two-particle state.

In the eikonal limit of  $p^+ = \infty$ , the value of  $\langle p_{\perp}^2(x^+) \rangle$  can be calculated exactly according to Eq. (27). The results from numerical simulation agree with such expectations, as shown in Fig. 11. In contrast to the small-separation quark-gluon state, which is shown in Fig. 7, the difference in the total momentum for different color configurations is negligible. This is because the quark and the gluon are too far away from each other, such that they are hardly correlated. Then, as shown in Fig. 12, at a finite  $p^+$  the quark-gluon correlation is still negligible.

Figure 13 presents the transverse momentum distribution  $p_{\perp} f(p_{\perp}) d p_{\perp}$  of the quark-gluon state in both the infinite and finite  $p^+$  cases. From here, we can see that there is no sizable difference between the total and the relative momenta, implying a vanishing quark-gluon correlation.

## C. The dressed quark state $|q\rangle + |qg\rangle$

We have studied the respective behaviors of a single quark state and a quark-gluon state in the preceding sections. In both cases, we find our numerics agree with the analytical expectation in the eikonal limit with a sufficiently large number of layers  $N_{\eta}$ . We now proceed to a more realistic and interesting scenario by allowing the quark to emit and absorb a gluon throughout the quenching process. We initialize the simulation with a single quark state of  $\vec{p}_{\perp} = \vec{0}_{\perp}$  in the  $|q\rangle + |qg\rangle$  space.

Specifically, by comparing the momentum broadening of the  $|q\rangle$  sector and the total, we could study the contribution from gluon emission to  $\hat{q}$ . For a dressed quark state, the momenta of each sector can be evaluated as the following

$$\begin{aligned} \langle p_{\perp}^2 \rangle_{|q\rangle} &= \langle q | p_{\perp}^2 | q \rangle / P_q, \\ \langle p_{\perp}^2 \rangle_{|qg\rangle} &= \sum_{k_g^+ = 1}^{K-1/2} \langle qg; k_g^+ | p_{\perp}^2 | qg; k_g^+ \rangle / P_{qg; k_g^+}, \end{aligned} \quad (32)$$

in which  $P_q$  is the probability of the state to be in the  $|q\rangle$ , and  $P_{qg; k_g^+}$  to be in the  $|qg\rangle$  sector, with the gluon

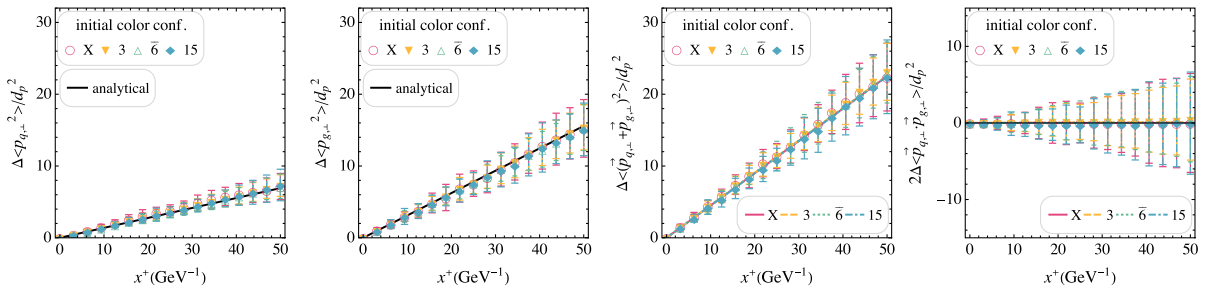


FIG. 11. The transverse momentum evolution of a large-separated quark-gluon state [distribution as shown in Fig. 6(b)] in the eikonal limit of  $p^+ = \infty$ . See simulation parameters and explanation of legends and data points in the caption of Fig. 7. The lines are analytical expectations at  $p^+ = \infty$  evaluated according to Eqs. (23) and (27).

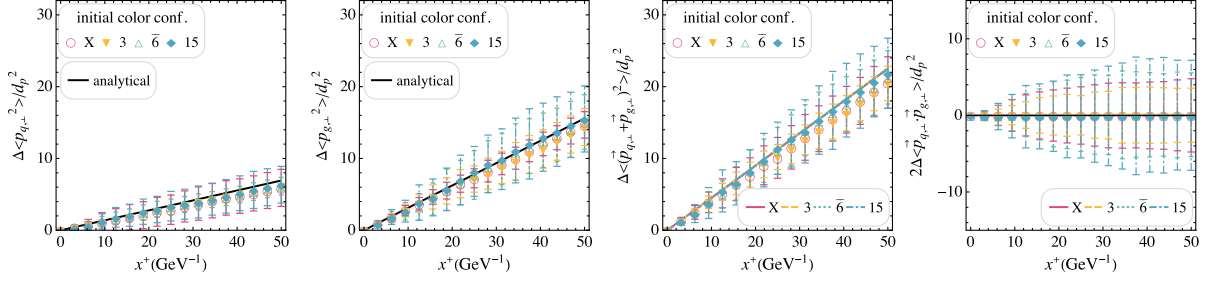


FIG. 12. The transverse momentum evolution of a large-separated quark-gluon state [distribution as shown in Fig. 6(b)] at  $p^+ = 1.5$  GeV ( $p_q^+ = 0.5$  GeV and  $p_g^+ = 1.0$  GeV) with  $m_q = 0.15$  GeV. See simulation parameters and explanation of legends and data points in the caption of Fig. 7. The lines are analytical expectations at  $p^+ = \infty$  evaluated according to Eqs. (23) and (27).

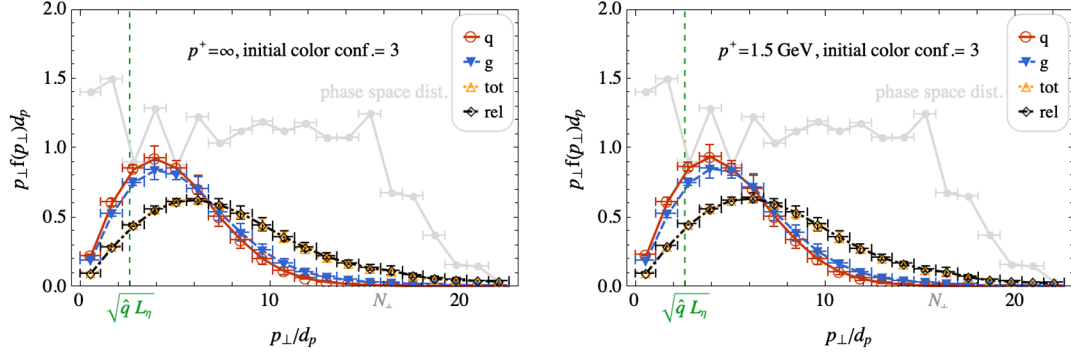


FIG. 13. The transverse momentum distribution  $p_{\perp} f(p_{\perp}) d_p$  of the long-separated color-triplet quark-gluon state at infinite and finite  $p^+$ , after the evolution through the medium, at  $x^+ = 50$  GeV $^{-1}$ . See simulation parameters and explanation of legends in the caption of Fig. 10.

longitudinal momentum fraction  $z = k_g^+/K$ . The total momentum is, therefore,

$$\langle p_{\perp}^2 \rangle_{\text{total}} = P_q \langle p_{\perp}^2 \rangle_{|q\rangle} + P_{|qg\rangle} \langle p_{\perp}^2 \rangle_{|qg\rangle}, \quad (33)$$

with

$$P_{|qg\rangle} \equiv \sum_{k_g^+=1}^{K-1/2} P_{qg;k_g^+}, \quad P_q + P_{|qg\rangle} = 1. \quad (34)$$

In order to understand the interplay of the medium scattering and the gluon emission, we run the simulation at various medium intensities (quantified by  $Q_s a_{\perp}/\pi$ ) and jet energies (quantified by  $p^+$ ).

Recall that the longitudinal ( $x^+$ ) structure of the medium, quantified by the boost invariance  $\tau/p^+$ , also has an effect on the jet momentum broadening, as we have discussed extensively in Sec. IV A 1. Here we explore the  $\tau/p^+ < 1$  regime, or in other words, the large- $N_{\eta}$  regime. This corresponds to the physics that the medium has infinite uncorrelated color charges along its longitudinal direction, allowing us to have analytically tractable limits to compare with.

Figure 14 shows the evolution of the a quark jet in the  $|q\rangle + |qg\rangle$  space in four different scenarios: Fig. 14(a) in vacuum with  $p^+ = 17.0$  GeV, Fig. 14(b) at  $Q_s a_{\perp}/\pi = 0.117$  and  $p^+ = 17.0$  GeV, Fig. 14(c) at  $Q_s a_{\perp}/\pi = 0.234$  and  $p^+ = 17.0$  GeV, and Fig. 14(d) at  $Q_s a_{\perp}/\pi = 0.117$  and  $p^+ = 8.5$  GeV. We take  $\tau = 3.125$  GeV $^{-1}$ , such that there are a number of  $N_{\eta} = 16$  layers of independent sources for the medium at  $x^+ = [0, L_{\eta} = 50 \text{ GeV}^{-1}]$ . The initial state is a single quark with  $\vec{p}_{\perp} = \vec{0}_{\perp}$  and  $p_Q^+ = p^+$ . For all configurations we plot the total  $p_{\perp}^2$  of the jet, and the probability to be in the original momentum mode in the  $|q\rangle$  sector, another  $|q\rangle$  mode or the  $|qg\rangle$  sector, and the probabilities for the different color states. We have the following key observations.

First, the inclusion of the  $|qg\rangle$  sector substantially enhances the jet momentum broadening. In all the three cases with medium shown in Fig. 14, the transverse momentum of the jet,  $\langle p_{\perp}^2 \rangle_{\text{total}}$ , increases at a larger rate than that of the single quark,  $\langle p_{\perp}^2 \rangle_{|q\rangle}$ . The former, by its definition, is a weighted sum of  $\langle p_{\perp}^2 \rangle_{|q\rangle}$  and  $\langle p_{\perp}^2 \rangle_{|qg\rangle}$ . We see that  $\langle p_{\perp}^2 \rangle_{|q\rangle}$  agrees with the analytical result calculated in the eikonal case of  $p^+ = \infty$ , Eq. (15), just as one would expect in the  $\tau/p^+ < 1$  regime. The momentum broadening of the  $|qg\rangle$  component resembles that of the  $|q\rangle$  initially and

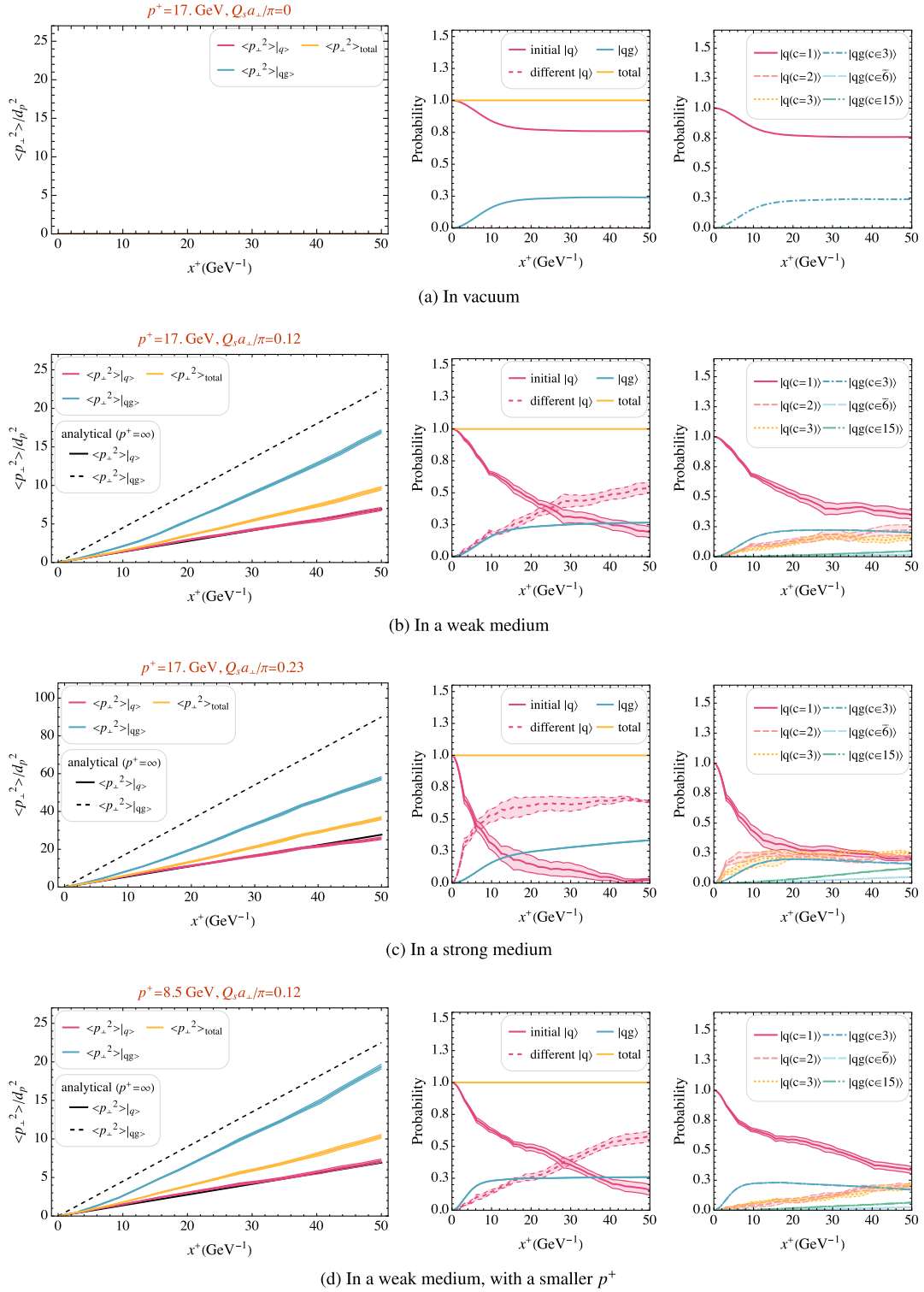


FIG. 14. The transverse momentum evolution of a quark jet in the  $|q\rangle + |qg\rangle$  space in vacuum and at different media and  $p^+$  (values indicated in each subfigure). The middle and the rightmost panels are the probability functions in the Fock and color phase space, respectively. The initial state is a single quark with  $\vec{p}_{\perp} = \vec{0}_{\perp}$  and  $p_Q^+ = p^+$ . Simulation parameters:  $N_{\perp} = 16$ ,  $L_{\perp} = 50 \text{ GeV}^{-1}$ ,  $\tau = 3.125 \text{ GeV}^{-1}$ , and  $K = 8.5$ . The analytical results at  $p^+ = \infty$  in the solid and dashed black lines are calculated according to Eq. (15).

gradually migrates to a much larger rate. The initial quarklike broadening is due to the fact that the  $|qg\rangle$  components appear by transiting from the  $|q\rangle$  sector, a process that conserves momentum. Later, when the occupation of the  $|qg\rangle$  components stabilizes, its momentum value reveals the effect of the direct medium interaction. Since the quark-gluon state has a larger color phase space, its momentum broadens at a larger rate than that of the single quark, due to the Casimir effect. The dashed black line shows the momentum broadening of a single  $|qg\rangle$  state, with a zero initial total transverse momentum, according to Eq. (23). Note that in this case, the quark and the gluon are spatially decorrelated; thus, the cross term is negligible, as we have seen in Sec. IV B. Overall, one can think that the jet momentum broadening in the  $|q\rangle + |qg\rangle$  Fock space is larger compared to that in  $|q\rangle$  due to the larger phase space.

Second, the medium interaction interferes with the gluon emission process. The medium is absent, relatively weak and strong in Figs. 14(a)–14(c), respectively. In the vacuum case, the  $|qg\rangle$  probability stabilizes at about  $x^+ = 20 \text{ GeV}^{-1}$ , and similarly in the case with a weaker medium. Consequently, in a weak medium,  $\langle p_{\perp}^2 \rangle_{|qg\rangle}$  increases almost at a constant rate, which is seen as the line almost in parallel with the dashed analytical line. Differently, in the stronger-medium case, the  $|qg\rangle$  probability is still increasing till the end of the evolution. As a result,  $\langle p_{\perp}^2 \rangle_{|qg\rangle}$  increases at a slower rate than the dashed analytical line because at each intermediate time instant, the newly generated  $|qg\rangle$  component broadens as a quark. The rightmost panels show the evolution in color space. The color configuration is dominated by the triplet states initially in all cases. The medium interaction results in the color transitions, as can be seen by comparing Figs. 14(b) and 14(c) to Fig. 14(a). The color transition is faster in a stronger medium by comparing Fig. 14(c) to Fig. 14(b). We summarize this effect as the following: the medium interaction enhances gluon emission by promoting the  $|qg\rangle$  occupation, which in return in fact slows down jet momentum broadening as compared to a pure  $|qg\rangle$  state.

Third, jet longitudinal momentum drags down the process of gluon emission. From Figs. 14(b) to 14(d), the jet  $p^+$  is halved, and the  $|qg\rangle$  probability stabilizes twice faster, at about  $x^+ = 10 \text{ GeV}^{-1}$ . Accordingly,  $\langle p_{\perp}^2 \rangle_{|qg\rangle}$  increases at the rate of a pure quark-gluon state much earlier, which is seen as its line in Fig. 14(d) is closer to the dashed analytical line than that in Fig. 14(b). Therefore, a smaller  $p^+$  leads to a larger jet momentum broadening.

To further examine the effect of gluon emission in the medium, we plot the probabilities of the  $|qg\rangle$  sector after evolution in the relatively weak and strong media in Fig. 15. Here, we also show the dependence on  $1/K$ , with  $K = 2.5, 4.5, 6.5, 7.5, 8.5$ . The leftmost data points are the same as those in Figs. 14(b) and 14(c). As we have observed in Fig. 14, now at each  $K$ , the  $|qg\rangle$  probability is higher in the stronger medium. On the other hand, as  $K$

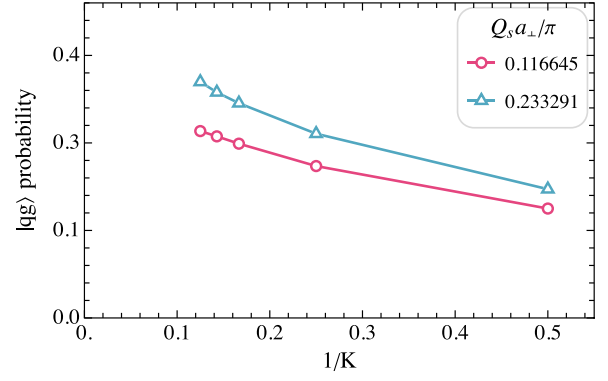


FIG. 15. The probabilities of the  $|qg\rangle$  sector after the evolution at various  $K$  and two different saturation scales, at  $x^+ = 50 \text{ GeV}^{-1}$ .

increases, the  $|qg\rangle$  probability also increases. This can be understood in the sense that as  $K$  increases, the resolution on longitudinal momentum fractions increases, and the available phase space for the  $|qg\rangle$  sector gets larger. In addition, the smallest value of  $z_g = 1/K$  also gets smaller as well, and the  $|q\rangle \rightarrow |qg\rangle$  process is largest around  $z_g = 0$ .<sup>5</sup> However, the total momentum square does not increase substantially when  $K$  increases from 2.5 to 8.5. The reason is that the different  $p^+$  segments of the  $|qg\rangle$  sector have approximately the same broadening effect caused by the medium, a process independent of  $p^+$ . Thus  $\langle p_{\perp}^2 \rangle_{|qg\rangle}$  is not sensitive to  $K$ . The contribution of  $K$  into  $\langle p_{\perp}^2 \rangle_{|qg\rangle}$  mainly comes from the probability  $P_{|qg\rangle}$  through Eq. (32). Our calculation is different from the study of keeping track of only one daughter particle (in our setup, this means counting the quark's instead of the total momentum of the  $|qg\rangle$  state), in which the recoil effects from other daughter particles can be large compared to the eikonal term [50,66]. Though in each time step, the splitting  $|q\rangle \rightarrow |qg\rangle$  favors the quark-gluon state with large relative transverse momentum (more discussions can be found in our previous work Ref. [29]), the total transverse momentum is conserved, and the recoil effect is not counted into  $\langle p_{\perp}^2 \rangle_{|qg\rangle}$ .

To quantify the medium-induced gluon emission, we define  $\delta P_{|qg\rangle}$  as the difference of the probability of the quark jet in the  $|qg\rangle$  sector in the medium and that in the vacuum,

$$\delta P_{|qg\rangle}(Q_s, x^+) \equiv P_{|qg\rangle}(Q_s, x^+) - P_{|qg\rangle}(Q_s = 0, x^+). \quad (35)$$

<sup>5</sup>At each small time step, it is true that the  $|q\rangle \rightarrow |qg\rangle$  process also favors the large  $z_g (\approx 1)$  modes, e.g.,  $V_{qg} \propto 1/z_g^{3/2}/(1-z_g)$  in the spin-non-flip case. But over a longer time span, the transition to those large  $z_g$  modes gets suppressed by the large fluctuation of the energy  $\Delta P_{KE}^- \propto 1/z_g/(1-z_g)$  whereas the small  $z_g$  modes survive. We refer to our preceding work [29] and its Fig. 17 for illustration.



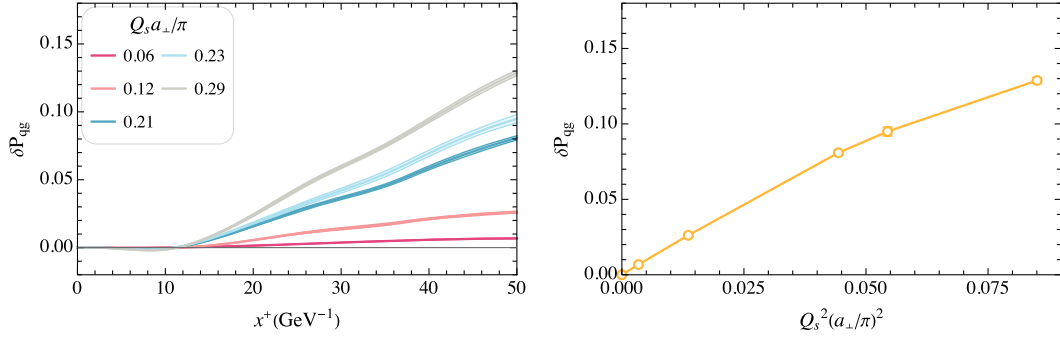


FIG. 16. The difference of the probability of the quark jet in the  $|qg\rangle$  sector in the medium and that in the vacuum, as defined in Eq. (35), as a function of evolution time  $x^+$  and saturation scale  $Q_s$ .

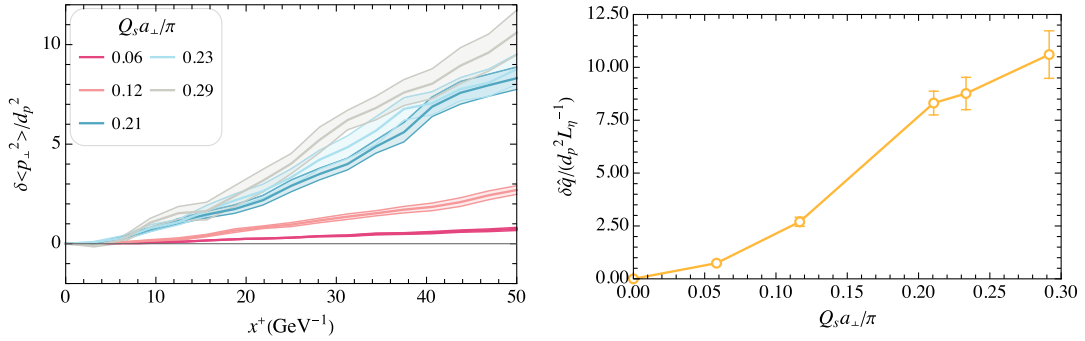


FIG. 17. The noneikonal correction to  $\hat{q}$  as defined in Eq. (36), as a function of evolution time  $x^+$  and saturation scale  $Q_s$ .

We present one set of results in Fig. 16, from simulations with the same parameters taken in Fig. 14, at  $p^+ = 17$  GeV. On the left panel, we see that the  $\delta P_{|qg\rangle}$ s at various saturation scale  $Q_s$  have a similar behavior: each curve forms a very small dip in the early time region, then after around the point  $x^+ = 12$  GeV $^{-1}$ , grows linearly in time. Comparing the curves at different  $Q_s$ , one can see that the denser the medium, the more the  $|qg\rangle$  component develops. This is also shown on the right panel, where the  $\delta P_{|qg\rangle}$  of the final state ( $x^+ = L_\eta = 50$  GeV $^{-1}$ ) is approximately proportional to  $Q_s^2$ . A similar observation has been made in Ref. [67], using the high-twist approach and agreeing with the Gyulassy-Levai-Vitev result in the first-order opacity expansion. There, the induced gluon radiation spectrum, counterpart to  $\delta P_{|qg\rangle}$  here, is proportional to the transverse-momentum gluon distribution density. Then the integration of such distribution's  $\langle \vec{p}_\perp^2 \rangle$  over the evolution time is the saturation scale  $Q_s^2$ .

It is also interesting to analyze the noneikonal and radiative correction to the quenching parameter  $\hat{q}$ . We define  $\delta\hat{q}$  as the difference of the  $\hat{q}$  that is calculated from the total momentum of the quark jet in the  $|q\rangle + |qg\rangle$  space, and the eikonal  $\hat{q}$  of a bare quark [as in Eq. (16)],

$$\delta\hat{q} \equiv \hat{q} - \hat{q}_{\text{Eik}}. \quad (36)$$

We present the results in Fig. 17, from the same set of simulations presented in Fig. 16. The left panel shows that  $\delta\langle p_\perp^2 \rangle (\equiv \langle p_\perp^2 \rangle - \langle p_\perp^2 \rangle_{\text{Eik}})$  increases over the evolution time at various  $Q_s$ . In the right panel, the  $\delta\hat{q}$  extracted from the final state  $\delta\langle p_\perp^2 \rangle$  is plotted, and it increases nontrivially when  $Q_s$  increases.

In summary, the momentum broadening of the quark jet in the  $|q\rangle + |qg\rangle$  Fock space is larger compared to that of the bare quark state  $|q\rangle$ , due to gluon emission. The difference between the two leads to a correction to  $\hat{q}$ .

## V. CONCLUSIONS

We present in this paper an extensive study on the momentum broadening of in-medium jet evolution using the tBLFQ approach. We perform the numerical simulation of the real-time jet evolution in the Fock space of  $|q\rangle$ ,  $|qg\rangle$ , and  $|q\rangle + |qg\rangle$ , at various jet energies  $p^+$  and medium densities. We obtain jet light-front wave function and we extract the jet transverse momentum distribution, the quenching parameter, and the gluon emission rate. We analyze the dependence of momentum broadening on  $p^+$ , medium density, color configuration, spatial correlation, and medium-induced gluon emission. For comparison, we also derive analytically in the eikonal limit the expectation value of the transverse momentum of a quark-gluon state for any color configuration and in an arbitrary spatial distribution.

This work provides an enhanced understanding of jet quenching beyond the eikonal limit. We have set up the initial quark projectile as a bare quark on its mass shell for the simplicity of the study. This setup is close to the scenario of a quark produced inside the medium from a hard scattering. This means that even in the vacuum, it will radiate gluons. In the language of our formalism, the bare quark is not an eigenstate of the full interacting Hamiltonian  $P_{KE}^- + V_{qg}$ . It only has a partial overlap with a dressed quark state, with the difference corresponding to vacuum radiation. This is possible because  $p^-$  need not be conserved at an interaction vertex, a convention known in the “old-fashioned perturbation theory” [68,69]. In a covariant formalism our initial quark should be thought of as an off-shell one, as required in order to have final state radiation and opposed to a quark on its mass shell that cannot emit gluons in the vacuum [10]. In this case, the four-momentum, including  $p^-$ , must be conserved at any interaction vertex, and the tradeoff is the initial quark being off shell.

A different and physically equally interesting scenario is the quark coming from outside the medium, described by the fully developed wave function that contains a gluon cloud [60]. We leave this task for our next work, where we will treat the initial quark as the eigenstate of the light-front QCD Hamiltonian in the  $|q\rangle + |qg\rangle$  space. Furthermore, the comparison of the two scenarios, with or without gluon-dressing initially, will also help reveal the relevance of intrinsic gluons in the initial state.

In our study, we consider the medium to be described by the MV model and keep the dominant field component at high energy  $\mathcal{A}^-$  in our calculation. This choice aligns with the approximation usually made in the eikonal picture of high-energy scattering. The inclusion of the transverse components of the background field is important to understand a class of subeikonal effects [70], which will introduce additional contributions to jet momentum broadening and transitions between helicity states. We intend to incorporate the transverse components to provide a more comprehensive analysis on jet evolution in future works.

## ACKNOWLEDGMENTS

We are very grateful to Guillaume Beuf, Fabio Dominguez, Miguel A. Escobedo, Xabier Feal, Sigtryggur Hauksson, Cyrille Marquet, Wenyang Qian, Andrecia Ramnath, Andrey Sadofyev, Konrad Tywoniuk, James P. Vary, Xin-Nian Wang, and Bin Wu for helpful and valuable discussions. X.Z. is supported by new faculty startup funding by the Institute of Modern Physics, Chinese Academy of Sciences, by Key Research Program of Frontier Sciences, Chinese Academy of Sciences, Grant No. ZDBS-LY-7020, by the Natural Science Foundation of Gansu Province, China, Grant No. 20JR10RA067, by the Foundation for Key Talents of Gansu Province, by the Central Funds Guiding the Local Science and Technology Development of Gansu Province, Grant No. 22ZY1QA006,

by international partnership program of the Chinese Academy of Sciences, Grant No. 016GJHZ2022103FN and by the Strategic Priority Research Program of the Chinese Academy of Sciences, Grant No. XDB34000000. M. L. and C. S. are supported by Xunta de Galicia (Centro singular de Investigacion de Galicia accreditation 2019-2022), European Union ERDF, the “Maria de Maeztu” Units of Excellence program under project CEX2020-001035-M, the Spanish Research State Agency under Project No. PID2020-119632 GB-I00, and European Research Council under Project No. ERC-2018-ADG-835105 YoctoLHC. T. L. is supported by the Academy of Finland, the Centre of Excellence in Quark Matter (Project No. 346324) and Project No. 321840. This work was also supported under the European Union’s Horizon 2020 research and innovation by the STRONG-2020 project (Grant Agreement No. 824093). The content of this article does not reflect the official opinion of the European Union and responsibility for the information and views expressed therein lies entirely with the authors.

## APPENDIX A: DISCRETIZATION

The conventions and notations in this paper follow Ref. [29]. We adopt the following shorthand notation for transverse integrals in position and momentum space, respectively,

$$\int_r \equiv \int d^2 r_\perp, \quad \int_p \equiv \int \frac{d^2 p_\perp}{(2\pi)^2}, \quad (\text{A1})$$

in which  $r_\perp = |\vec{r}_\perp|$  and  $p_\perp = |\vec{p}_\perp|$ . On the discrete basis space, the integrations become summations over the corresponding transverse quantum numbers ( $\vec{r}_\perp = \{n_1, n_2\}a_\perp$  and  $\vec{p}_\perp = \{k_1, k_2\}d_p$ ),

$$\sum_r \equiv a_\perp^2 \sum_{n_1, n_2 = -N_\perp}^{N_\perp-1}, \quad \sum_p \equiv \frac{1}{(2L_\perp)^2} \sum_{k_1, k_2 = -N_\perp}^{N_\perp-1}. \quad (\text{A2})$$

### 1. The transverse distribution function

In studying the angularly integrated transverse distribution function  $f(p_\perp)$  (recall that  $p_\perp = |\vec{p}_\perp| = |\mathbf{p}|$ ) and similarly its Fourier transform  $\tilde{f}(r_\perp)$  ( $r_\perp = |\vec{r}_\perp| = |\mathbf{r}|$ ), one needs to be aware that the phase space of states on the discrete square lattice is different from that in the continuous case. As  $p_\perp$  increases, the number of momentum modes within the range  $p_\perp \sim p_\perp + \delta_p$  (with  $\delta_p$  a small positive value) first increases up till the edge of the lattice  $\Lambda_{UV}$  and then drop down, whereas the continuous phase space would keep increasing as  $2\pi p_\perp \delta_p$ .

The 2D transverse distribution function  $f(\vec{p}_\perp)$  can be obtained directly by squaring the wave function  $|\psi(\vec{p}_\perp)|^2$ . The normalization is therefore  $\sum_p f(\vec{p}_\perp) = 1$  and

$\int_{\vec{p}} f(\vec{p}_\perp) = 1$  in the discrete and continuous case, respectively. By integrating/summing over the azimuthal angle,  $f(\vec{p}_\perp)$  becomes the 1D distribution function  $f(p_\perp)$ , the average value of  $f(\vec{p}_\perp)$  over momenta with the same  $p_\perp$ . In the continuous space, the normalization reads  $\int_{\vec{p}} f(\vec{p}_\perp) = \int p_\perp dp_\perp f(p_\perp)/(2\pi) = 1$ . To obtain  $f(p_\perp)$  from a distribution on the square lattice, we first group  $f(\vec{p}_\perp)$  into adjacent bins with equal span on  $p_\perp$ , then take the average value of the data in each bin as  $f(p_\perp)$ .

To be specific, choosing  $N_b$  as the total number of bins in the radial direction, then the dimensionless width of each bin is  $\omega_b = \sqrt{2}N_\perp/N_b$ . The dimensional bin width is  $\omega_b d_p$  and  $\omega_b a_\perp$  for the momentum and coordinate space, respectively. The  $i_b$ th bin would contain all the states with  $p_\perp/d_p(r_\perp/a_\perp) \in [i_b - 1, i_b)\omega_b$ ; note that states on the bin boundary should be counted only into one bin. Next, count the number of states in each bin,  $h(i_b)$ , and they should sum up as

$$\sum_{i_b=1}^{N_b} h(i_b) = (2N_\perp)^2. \quad (\text{A3})$$

The normalization in terms of the summation reads

$$\sum_{\vec{p}} f(\vec{p}_\perp) = \frac{1}{(2L_\perp)^2} \sum_{i_b=1}^{N_b} h(i_b) f(p_\perp) = 1. \quad (\text{A4})$$

Here,  $p_\perp(i_b) = (i - 1/2)\omega_b d_p$  inside the summation over bins, the center point of the  $i_b$ th bin. Similarly in the conjugate  $\vec{r}_\perp$  space, with  $h(i_b)$  the number of states in the  $i_b$ th bin along  $r_\perp$ ,

$$\sum_{\vec{r}} \tilde{f}(\vec{r}_\perp) = a_\perp^2 \sum_{i_b=1}^{N_b} h(i_b) \tilde{f}(r_\perp) = 1, \quad (\text{A5})$$

where  $r_\perp(i_b) = (i - 1/2)\omega_b a_\perp$ .

With  $h(i_b)$ , we can quantify the ratio between the discrete and the continuous space size at each bin, that is,  $h(i_b)d_p^2/(2\pi p_\perp d_p)$  [ $h(i_b)a_\perp^2/(2\pi r_\perp a_\perp)$ ] in the momentum (coordinate) space. With a simplification, it reads

$$R(i_b) \equiv \frac{h(i_b)}{2\pi(i - 1/2)\omega_b}. \quad (\text{A6})$$

This ratio function depends on the lattice size  $N_\perp$  and the number of bins  $N_b$ . Since  $i_b$  corresponds to a specific range of  $p_\perp$  or  $r_\perp$ , one can also write  $R$  in terms of  $p_\perp$  or  $r_\perp$ . Figure 18 exemplifies the behavior of  $R(p_\perp)/\omega_b$  at  $N_\perp = 16$  and at various  $N_b$ . The horizontal error bar indicates the range covered by each bin. The ratio function is overall flat when the momentum mode is below  $N_\perp$ , and decreases when going above. This is expected from the above discussion on  $h(i_b)$ . In addition, as  $N_b$  increases, the ratio function admits more ‘‘zigzag’’ patterns. With  $R$ , the normalization of the probability function is written as

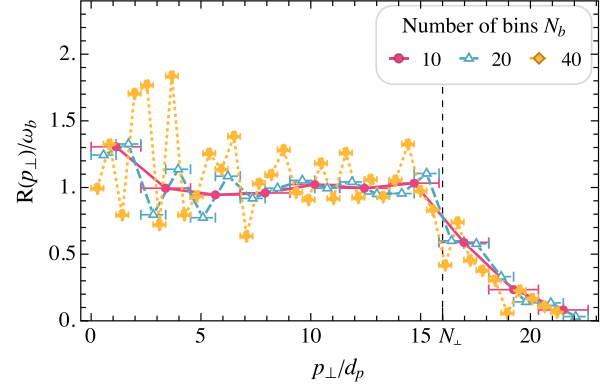


FIG. 18. The ratio function  $R(p_\perp)$  [as in Eq. (A6)] divided by bin width  $\omega_b$ , at  $N_\perp = 16$  and at various  $N_b$ .

$$\begin{aligned} \frac{1}{2\pi} \sum_{p_\perp} R(p_\perp) p_\perp f(p_\perp) d_p &= 1, \\ 2\pi \sum_{r_\perp} R(r_\perp) r_\perp \tilde{f}(r_\perp) a_\perp &= 1. \end{aligned} \quad (\text{A7})$$

## 2. Numerical simulation of the medium

In the discrete basis space, the correlation relation of the color charge in Eq. (2) takes the form,

$$\langle \rho_a(n^x, n^y, n_\tau) \rho_b(n'^x, n'^y, n'_\tau) \rangle_m = g^2 \tilde{\mu}^2 \delta_{ab} \frac{\delta_{n^x, n'^x} \delta_{n^y, n'^y} \delta_{n_\tau, n'_\tau}}{a_\perp^2 \tau}, \quad (\text{A8})$$

as we have implemented in Refs. [28,29]. The sources generating the medium are stochastic random variables with a Gaussian distribution on each site, with the transverse indices  $n^x, n^y = -N_\perp, -N_\perp + 1, \dots, N_\perp - 1$ , and the layer indices  $n_\tau = 1, 2, \dots, N_\eta$ .

Then  $\mathcal{A}$ , the field of the medium is solved from Eq. (3), a Poisson's equation in the two dimensions for each  $x^+$  layer. Numerically, it is efficient to solve in the momentum space, accompanied by a Fourier transform,

$$\begin{aligned} \mathcal{A}_a^-(n^x, n^y, x^+) &= \frac{1}{(2N_\perp)^2} \sum_{\bar{n}_x, \bar{n}_y = -N_\perp}^{N_\perp-1} \rho_a(\bar{n}^x, \bar{n}^y, n_\tau(x^+)) \\ &\times \sum_{k_x, k_y = -N_\perp}^{N_\perp-1} \frac{e^{-i[(n_x - \bar{n}_x)k_x + (n_y - \bar{n}_y)k_y]\pi/N_\perp}}{m_g^2 a_\perp^2 / \pi^2 / N_\perp^2 + k_x^2 + k_y^2}. \end{aligned} \quad (\text{A9})$$

We write  $n_\tau(x^+)$  to indicate that the larger indices  $n_\tau$  can be determined by the position of  $x^+$  in the entire duration of  $[0, L_\eta]$ . For each layer,  $\rho$  is sampled independently, so the resulting  $\mathcal{A}^-$  is also independent.

### APPENDIX B: AN ALTERNATIVE DERIVATION OF $\hat{q}$

Here we demonstrate an alternative derivation of the single particle quenching parameter in Eq. (16). Starting from Eqs. (12) and (13), we have

$$\langle p_{\perp}^2(x^+) \rangle_{\text{Eik}} = \int_{\mathbf{p}} \vec{p}_{\perp}^2 \int_{\mathbf{y}, \mathbf{r}} \tilde{\phi}^*(\vec{r}_{\perp} + \vec{y}_{\perp}) \tilde{\phi}(\vec{y}_{\perp}) e^{-i\vec{p}_{\perp} \cdot \vec{r}_{\perp}} \times S_F(0, x^+; r), \quad (\text{B1})$$

with a change of variables  $\vec{r}_{\perp} = \vec{x}_{\perp} - \vec{y}_{\perp}$  and  $r = |\vec{r}_{\perp}|$ . We first expand the Wilson line correlator,

$$S_F(0, x^+; r) = \sum_{n=0}^{\infty} \frac{1}{n!} (-C_F g^4 \tilde{\mu}^2 L(0) x^+)^n \left[ 1 - \frac{L(r)}{L(0)} \right]^n = \sum_{n=0}^{\infty} \frac{1}{n!} \left( -\frac{C_F g^4 \tilde{\mu}^2}{4\pi m_g^2} x^+ \right)^n \sum_{k=0}^n \binom{n}{k} \left[ -\frac{L(r)}{L(0)} \right]^k. \quad (\text{B2})$$

Next, we evaluate the integral for the power terms of  $L(r)$ ,

$$\begin{aligned} & \int_{\mathbf{p}} \vec{p}_{\perp}^2 \int_{\mathbf{r}, \mathbf{y}} \tilde{\phi}^*(\vec{r}_{\perp} + \vec{y}_{\perp}) \tilde{\phi}(\vec{y}_{\perp}) e^{-i\vec{p}_{\perp} \cdot \vec{r}_{\perp}} L(r)^m \\ &= \int_{\mathbf{p}} \vec{p}_{\perp}^2 \int_{l_1} \int_{l_2} \cdots \int_{l_m} \int_{\mathbf{r}, \mathbf{y}} \tilde{\phi}^*(\vec{r}_{\perp} + \vec{y}_{\perp}) \tilde{\phi}(\vec{y}_{\perp}) e^{-i(\vec{p}_{\perp} + \sum_{i=1}^m \vec{l}_{\perp, i}) \cdot \vec{r}_{\perp}} \left[ \prod_{j=1}^m \frac{1}{(m_g^2 + \vec{l}_{\perp, j}^2)^2} \right], \\ &= \int_{\mathbf{p}} \vec{p}_{\perp}^2 \int_{l_1} \int_{l_2} \cdots \int_{l_m} \phi^* \left( \vec{p}_{\perp} + \sum_{i=1}^m \vec{l}_{\perp, i} \right) \phi \left( \vec{p}_{\perp} + \sum_{i=1}^m \vec{l}_{\perp, i} \right) \left[ \prod_{j=1}^m \frac{1}{(m_g^2 + \vec{l}_{\perp, j}^2)^2} \right], \\ &= \int_{\mathbf{q}} \int_{l_1} \int_{l_2} \cdots \int_{l_m} \left( \vec{q}_{\perp} - \sum_{i=1}^m \vec{l}_{\perp, i} \right)^2 \phi^*(\vec{q}_{\perp}) \phi(\vec{q}_{\perp}) \left[ \prod_{j=1}^m \frac{1}{(m_g^2 + \vec{l}_{\perp, j}^2)^2} \right]. \end{aligned} \quad (\text{B3})$$

In the third line, the integral over  $\mathbf{r}$  and  $\mathbf{y}$  apply a Fourier transform to the wave functions, bringing them to the momentum space. In the last line, we made a change of variable  $\vec{q}_{\perp} \equiv \vec{p}_{\perp} + \sum_{i=1}^m \vec{l}_{\perp, i}$ . There are three terms coming from the square  $(\dots)^2$ . The first term containing  $\vec{q}_{\perp}^2$ , gives the transverse momentum squared of the initial state,

$$I_0(m) \equiv \int_{\mathbf{q}} \vec{q}_{\perp}^2 \phi^*(\vec{q}_{\perp}) \phi(\vec{q}_{\perp}) \left[ \prod_{i=1}^m \int_{l_i} \frac{1}{(m_g^2 + \vec{l}_{\perp, i}^2)^2} \right], = \langle p_{\perp}^2(0) \rangle L(0)^m, \quad (\text{B4})$$

in which the  $l_{\perp, i}$  integral gives  $L(0) = 1/(4\pi m_g^2)$ , according to Eq. (14).

The second term, containing  $\vec{q}_{\perp} \cdot \sum_i \vec{l}_{\perp, i}$ , vanishes after integrating over the angle of  $\vec{l}_{\perp, i}$ ,

$$\int_0^{2\pi} d\theta_i \frac{l_i \cos(\theta_i - \theta_q)}{(m_g^2 + \vec{l}_{\perp, i}^2)^2} = 0, \quad (\text{B5})$$

where  $\theta_i$  ( $\theta_q$ ) is the angle of the vector  $\vec{l}_{\perp, i}$  ( $\vec{q}_{\perp}$ ).

The last term, containing  $(\sum_i \vec{l}_{\perp, i})^2$ , reads

$$\begin{aligned} I_1(m) &\equiv \int_{\mathbf{q}} \phi^*(\vec{q}_{\perp}) \phi(\vec{q}_{\perp}) \int_{l_1} \int_{l_2} \cdots \int_{l_m} \left( \sum_{i=1}^m \vec{l}_{\perp, i} \right)^2 \\ &\quad \times \left[ \prod_{j=1}^m \frac{1}{(m_g^2 + \vec{l}_{\perp, j}^2)^2} \right], \\ &= \int_{l_1} \int_{l_2} \cdots \int_{l_m} \sum_{i=1}^m \vec{l}_{\perp, i}^2 \left[ \prod_{j=1}^m \frac{1}{(m_g^2 + \vec{l}_{\perp, j}^2)^2} \right], \\ &= \sum_{i=1}^m \int_{l_i} \frac{\vec{l}_{\perp, i}^2}{(m_g^2 + \vec{l}_{\perp, i}^2)^2} \left[ \prod_{j \neq i} \int_{l_j} \frac{1}{(m_g^2 + \vec{l}_{\perp, j}^2)^2} \right], \\ &= m \mathcal{G}_2 L(0)^{m-1}. \end{aligned} \quad (\text{B6})$$

The  $\mathbf{q}$  integral is the normalization of the initial state wave function, thus giving unity. The cross term  $\vec{l}_{\perp, i} \cdot \vec{l}_{\perp, k}$  vanishes after the angular integral, as in Eq. (B5). The  $l_{\perp, i}$  integral is logarithmically divergent, introducing a pair of IR and UV cutoffs,

$$\begin{aligned} \mathcal{G}_2 &\equiv \int_p \frac{\vec{p}_\perp^2}{(m_g^2 + \vec{p}_\perp^2)^2} = \int_{\lambda_{\text{IR}}}^{\lambda_{\text{UV}}} \frac{dp}{2\pi} \frac{p^3}{(m_g^2 + p^2)^2}, \\ &= \frac{1}{4\pi} \left[ \log \left( \frac{\lambda_{\text{UV}}^2 + m_g^2}{\lambda_{\text{IR}}^2 + m_g^2} \right) - m_g^2 \left( \frac{1}{\lambda_{\text{IR}}^2 + m_g^2} - \frac{1}{\lambda_{\text{UV}}^2 + m_g^2} \right) \right]. \end{aligned} \quad (\text{B7})$$

In the numerical calculation, one should always let  $\lambda_{\text{IR}} \ll m_g$ , such that the result does not depend on the numerical cutoff  $\lambda_{\text{IR}}$ , and  $m_g$  plays the role of the IR regulator,

$$\mathcal{G}_2|_{\lambda_{\text{IR}}=0} = \frac{1}{4\pi} \left[ \log \left( \frac{\lambda_{\text{UV}}^2 + m_g^2}{m_g^2} \right) - \frac{\lambda_{\text{UV}}^2}{\lambda_{\text{UV}}^2 + m_g^2} \right]. \quad (\text{B8})$$

We thereby obtain Eq. (17).

Back to Eq. (B1), we have

$$\begin{aligned} \langle p_\perp^2(x^+) \rangle_{\text{Eik}} &= \sum_{n=0}^{\infty} \frac{1}{n!} \left( -\frac{C_F g^4 \tilde{\mu}^2}{4\pi m_g^2} x^+ \right)^n \sum_{k=0}^n \binom{n}{k} (-1)^k \\ &\quad \times \left[ \langle p_\perp^2(0) \rangle + k \mathcal{G}_2 \frac{1}{L(0)} \right], \\ &= \langle p_\perp^2(0) \rangle + \mathcal{G}_2 C_F g^4 \tilde{\mu}^2 x^+. \end{aligned} \quad (\text{B9})$$

We have used the following relations in the above equation,

$$\sum_{k=0}^n \binom{n}{k} (-1)^k = \delta_{n,0}, \quad \sum_{k=0}^n \binom{n}{k} (-1)^k k = -\delta_{n,1}. \quad (\text{B10})$$

From here, we see that only the linear term survives in the acquired momentum, and we arrive at the result of  $\hat{q}$  in Eq. (16).

### APPENDIX C: THE COLOR DIMENSION OF THE QUARK-GLUON STATE

In this appendix, we first present two sets of the basis for the quark-gluon color space and the transformation between the two. Then, we write out the antiquark-gluon-quark-gluon color singlet states. This transformation is helpful in deriving the four-point Wilson line correlators.

#### 1. The quark-gluon color states

The color space of the quark-gluon state is the tensor product of the color spaces of a single quark and a single gluon. This 24-dimensional space, built up as a product of a triplet and an octet, reduces into a direct sum of three irreducible representations,

$$3 \otimes 8 = 3 \oplus \bar{6} \oplus 15. \quad (\text{C1})$$

This is a Clebsch-Gordan (CG) series of SU(3), and can be obtained from the Young tableaux method, e.g., see Chapter 12 of Ref. [71]. For the generalization to SU( $N_c$ ), we still take 3, 8,  $\bar{6}$ , and 15, as the names of the corresponding representations, for convenience. We use  $\dim(R)$  to denote the dimension of the  $R$  representation, such that  $\dim(3) = N_c$ ,  $\dim(8) = N_c^2 - 1$ ,  $\dim(\bar{6}) = N_c(N_c + 1)(N_c - 2)/2$ , and  $\dim(15) = N_c(N_c - 1)(N_c + 2)/2$ .

The two representations, given on the left- and right-hand sides of Eq. (C1), provide us with two bases for the quark-gluon color state. The uncoupled color basis is indexed by iterating the quark and gluon color, in the tuple form as  $[c_q, c_g]$  ( $c_q = 1, 2, 3, c_g = 1, 2, \dots, 8$ ), or in the number form as  $c_{qg} = (c_q - 1) \times 8 + c_g$  in which  $c_g$  is iterated over first. This uncoupled basis is convenient for simulating the interaction between an individual particle and the background field, as we have adopted in formulating the numerical calculations [29]. The coupled color basis is indexed by enumerating the representations in the right-hand side  $\{h_{qg}\}$ .

The basis expansion of a  $|qg\rangle$  color state on the two bases are, respectively,

$$\begin{aligned} |\psi\rangle &= \sum_{c_q=1}^3 \sum_{c_g=1}^8 \langle c_q, c_g | \psi \rangle |c_q, c_g\rangle = \sum_{i=1}^{24} \alpha_i |c_{qg} = i\rangle, \\ |\psi\rangle &= \sum_{h_{qg}=1}^{24} \langle h_{qg} | \psi \rangle |h_{qg}\rangle = \sum_{j=1}^{24} \beta_j |h_{qg} = j\rangle. \end{aligned} \quad (\text{C2})$$

In the above equation,  $\alpha_i$  is the coefficient of the wave function in the uncoupled basis, and  $\beta_j$  in the coupled basis. Their column vector forms are  $\boldsymbol{\alpha}$  and  $\boldsymbol{\beta}$ , respectively. The transformations between the two bases are specified by the SU(3) CG coefficients,  $\mathcal{C}(h_{qg}; c_q, c_g)$ ,

$$\begin{aligned} |h_{qg}\rangle &= \sum_{c_q=1}^3 \sum_{c_g=1}^8 \mathcal{C}(h_{qg}; c_q, c_g) |c_q, c_g\rangle, \\ |c_q, c_g\rangle &= \sum_{h_{qg}=1}^{24} \mathcal{C}^{-1}(h_{qg}; c_q, c_g) |h_{qg}\rangle. \end{aligned} \quad (\text{C3})$$

Writing the CG coefficients  $\mathcal{C}(h_{qg}; c_q, c_g)$  in the matrix form  $\mathcal{C}$  with row index  $h_{qg}$  and column index  $c_{qg}(c_q, c_g)$ , we see that  $\boldsymbol{\alpha} = \mathcal{C}\boldsymbol{\beta}$ . The transformation matrix is unitary,  $\mathcal{C}^{-1} = \mathcal{C}^\dagger$ . For convenience, we partition  $\mathcal{C}$  into blocks  $\mathcal{C} = \{\mathcal{C}_Q, \mathcal{C}_{h6}, \mathcal{C}_{h15}\}^\dagger$  such that the three operators extract the 3, the  $\bar{6}$ , and the 15 components of a state, respectively.

There are multiple ways of computing  $\mathcal{C}$ , and here we proceed with the tensor method as illustrated in Ref. [71]. The generic quark-gluon state is described by a tensor,

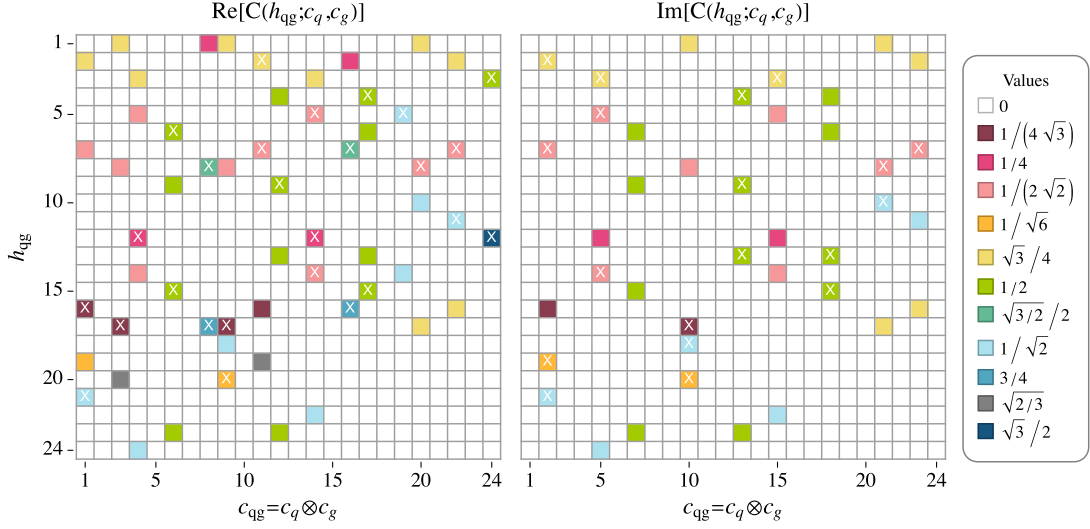


FIG. 19. The CG coefficients  $\mathcal{C}(h_{qg}; c_q, c_g)$  as defined in Eq. (C3). The white cross indicates negative values in the corresponding grids.

$$\begin{aligned}
 u^i v_k^j &= \frac{1}{8} (3\delta_k^i u^l v_l^j - \delta_k^l u^l v_l^j) \\
 &+ \frac{1}{4} \epsilon^{ijk} (\epsilon_{lmn} u^m v_k^n + \epsilon_{kmn} u^m v_l^n) \\
 &+ \frac{1}{2} \left( u^i v_k^j + u^j v_k^i - \frac{1}{4} \delta_k^i u^l v_l^j - \frac{1}{4} \delta_k^j u^l v_l^i \right), \quad (C4)
 \end{aligned}$$

which acts in the tensor product space  $|i\rangle|j\rangle|k\rangle$ . It relates to the uncoupled quark-gluon basis by the Gell-Mann matrices  $|c_q = i, c_g = a\rangle = T_{kj}^a |i\rangle|j\rangle|k\rangle$ . The right-hand side is the CG decomposition, and the three terms correspond to the quark-gluon in the 3, the  $\bar{6}$ , and the 15 state, respectively. We thereby find the transformation between the uncoupled and the coupled states. However, the transformation matrix is expressed in the tensor representation. The transformations to the states in the triplet,  $h_{qg} = c_Q = 1, 2, 3$ , are given by the Gell-Mann matrices,

$$\mathcal{C}_Q(h_{qg} = c_Q; c_q, c_g) = \frac{\sqrt{3}}{2} T_{c_q, c_g}^{c_Q}. \quad (C5)$$

The coefficient is determined by state normalization. The transformations to the states in the antisextet are specified by two symmetric indices  $m, n = 1, 2, 3$ ,

$$\tilde{\mathcal{C}}_{h6}(m, n; i, a) = \frac{1}{2} \sum_j^3 (T_{nj}^a \epsilon_{ijm} + T_{mj}^a \epsilon_{ijn}). \quad (C6)$$

The  $\{m, n\}$  states must be related to the coupled states  $h_{qg} = 4, \dots, 9$  by some linear combination, thus  $\mathcal{C}_{h6}(h_{qg}; c_q, c_g) = \sum_{m,n=1}^3 h_{qg}(m, n) \tilde{\mathcal{C}}_{h6}(m, n; c_q, c_g)$ . The transformations to the 15-plet states are specified by three indices  $\bar{i}, \bar{j}, \bar{k} = 1, 2, 3$ ,

$$\begin{aligned}
 \tilde{\mathcal{C}}_{h15}(\bar{i}, \bar{j}, \bar{k}; i, a) \\
 = \frac{\sqrt{2}}{2} \left( T_{\bar{k}j}^a \delta_{\bar{i}}^i + T_{\bar{k}\bar{i}}^a \delta_{\bar{j}}^j - \frac{1}{4} T_{ij}^a \delta_{\bar{k}}^{\bar{k}} - \frac{1}{4} T_{\bar{i}\bar{j}}^a \delta_{\bar{k}}^{\bar{k}} \right). \quad (C7)
 \end{aligned}$$

The  $\{\bar{i}, \bar{j}, \bar{k}\}$  states must be related to the coupled states  $h_{qg} = 10, \dots, 24$  by some linear combination, thus  $\mathcal{C}_{h15}(h_{qg}; c_q, c_g) = \sum_{\bar{i}, \bar{j}, \bar{k}=1}^3 h_{qg}(\bar{i}, \bar{j}, \bar{k}) \tilde{\mathcal{C}}_{h15}(\bar{i}, \bar{j}, \bar{k}; c_q, c_g)$ . The specific form of  $h_{qg}(m, n)$  and  $h_{qg}(\bar{i}, \bar{j}, \bar{k})$  depends on the choice of the coupled basis states. We provide here one set of  $\mathcal{C}$  in Fig. 19. We construct it by an online CG coefficients generator [72] based on the numerical algorithm proposed in Ref. [73].<sup>6</sup>

It is also useful to define the projectors, using the transformation matrix  $\mathcal{C}$ , or equivalently  $\tilde{\mathcal{C}}$  in the tensor product basis,

$$\begin{aligned}
 \mathbf{P}_Q &= \mathcal{C}_Q^{-1} \mathbf{C}_Q, \\
 \mathbf{P}_{h6} &= \mathcal{C}_{h6}^{-1} \mathbf{C}_{h6} = \tilde{\mathcal{C}}_{h6}^{-1} \tilde{\mathcal{C}}_{h6}, \\
 \mathbf{P}_{h15} &= \mathcal{C}_{h15}^{-1} \mathbf{C}_{h15} = \tilde{\mathcal{C}}_{h15}^{-1} \tilde{\mathcal{C}}_{h15}. \quad (C8)
 \end{aligned}$$

The expectation value of each projector operator  $\langle \psi | \mathbf{P} | \psi \rangle$  gives the probability of the state in the corresponding color subspace. In the component form,  $\mathbf{P}|_{j,b;i,a} = \sum_{\{s\}} \mathcal{C}^{-1}(j, b; \{s\}) \mathcal{C}(\{s\}; I, a)$ , in which the summation is over the full basis space indexed by  $\{s\}$ . One can find the

<sup>6</sup>Note, however, the CG coefficients obtained directly from Ref. [72] are in the Gelfand-Tsetlin basis (cf. the Cartan-Weyl basis, see Ref. [73] for more details), not on the Gell-Mann basis that one usually adopts in high-energy physics, this work as well. An easy way to find the transformation from the Gelfand-Tsetlin to the Gell-Mann basis is by comparing the CG coefficients for the known decomposition  $3 \otimes \bar{3} = 1 \oplus 8$ .

projectors using Eqs. (C5)–(C7). Here, we write out the expressions for  $SU(N_c)$  [74,75],

$$\mathbf{P}_Q|_{j,b;i,a} = \frac{2N_c}{N_c^2 - 1} (T^a T^b)_{ij}, \quad (\text{C9a})$$

$$\mathbf{P}_{h6}|_{j,b;i,a} = \frac{1}{2} \delta_{ab} \delta_{ij} - (T^b T^a)_{ij} - \frac{1}{N_c - 1} (T^a T^b)_{ij}, \quad (\text{C9b})$$

$$\mathbf{P}_{h15}|_{j,b;i,a} = \frac{1}{2} \delta_{ab} \delta_{ij} + (T^b T^a)_{ij} - \frac{1}{N_c + 1} (T^a T^b)_{ij}. \quad (\text{C9c})$$

The summation of those projectors is identity, as should be,  $\mathbf{I}_{N_f \times N_A} = \mathbf{P}_Q + \mathbf{P}_{h6} + \mathbf{P}_{h15}$ .

## 2. The antiquark-gluon-quark-gluon color singlet states

In the full color space of  $\bar{q} \otimes \bar{g} \otimes q \otimes g$ , there are three singlets,  $\bar{3} \otimes 8 \otimes 3 \otimes 8 = 1 \oplus 1 \oplus 1 \oplus 8 \oplus \dots$ . We consider two sets of basis in this singlet subspace, namely, the  $s$  basis, and the  $v$  basis, as illustrated in Fig. 20. The  $s$  basis as an expansion in the uncoupled basis space reads

$$\begin{aligned} |s_1\rangle &= -\sqrt{\frac{1}{N_c d_A}} \sum_{i,j=1}^{N_c} \sum_{a,b=1}^{d_A} \delta_{i,j} \delta_{a,b} |i, a, j, b\rangle, \\ |s_2\rangle &= \frac{1}{i} \sqrt{\frac{2}{N_c d_A}} \sum_{i,j=1}^{N_c} \sum_{a,b=1}^{d_A} f_{abc} T_{ji}^c |i, a, j, b\rangle, \\ |s_3\rangle &= \sqrt{\frac{2}{C_d d_A}} \sum_{i,j=1}^{N_c} \sum_{a,b=1}^{d_A} d_{abc} T_{ji}^c |i, a, j, b\rangle, \end{aligned} \quad (\text{C10})$$

in which  $d_A = N_c^2 - 1 = 8$ ,  $C_d = (N_c^2 - 4)/N_c = 5/3$ ,  $d_{abc} = 2\text{Tr}[\{T_a, T_b\}T_c]$ , and  $f_{abc} = -2i\text{Tr}[[T_a, T_b]T_c]$ . The convention in defining the  $s$  basis is the same as those in Ref. [64], by replacing two  $\bar{q}q$  dipoles by two gluons, viz.,  $|c_g\rangle = \sqrt{2} \sum_{\bar{c}_q, c_q} T_{c_q, \bar{c}_q}^c |c_q, c_q\rangle$ .

The  $v$  basis as an expansion in the uncoupled basis space can be written in terms of the  $qg$  projectors defined in Eq. (C8),

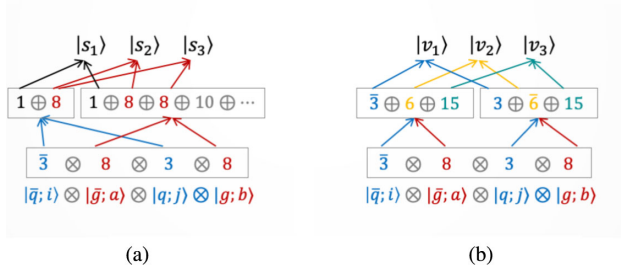


FIG. 20. An illustration of constructing the color singlet subspace of the  $\bar{q} \otimes \bar{g} \otimes q \otimes g$  state into (a) the  $s$  basis as in Eq. (C10) and (b) the  $v$  basis as in Eq. (C11).

$$|v_1\rangle = \frac{1}{\sqrt{\dim(3)}} \sum_{i,j=1}^{N_c} \sum_{a,b=1}^{d_A} \mathbf{P}_Q |i,a;j,b\rangle |i, a, j, b\rangle,$$

$$|v_2\rangle = \frac{1}{\sqrt{\dim(6)}} \sum_{i,j=1}^{N_c} \sum_{a,b=1}^{d_A} \mathbf{P}_{h6} |i,a;j,b\rangle |i, a, j, b\rangle,$$

$$|v_3\rangle = \frac{1}{\sqrt{\dim(15)}} \sum_{l=1}^{15} \sum_{a,b=1}^{d_A} \mathbf{P}_{h15} |i,a;j,b\rangle |i, a, j, b\rangle. \quad (\text{C11})$$

The transformation between the two bases is

$$|v_I\rangle = \sum_{J=1}^3 |s_J\rangle \langle s_J | v_I\rangle, \quad |s_I\rangle = \sum_{J=1}^3 |v_J\rangle \langle v_J | s_I\rangle, \quad (\text{C12})$$

for which we write out the transformation matrix  $V$  with element  $V_{JI} = \langle s_J | v_I\rangle = \langle v_I | s_J\rangle$ ,

$$\begin{aligned} V &= \begin{pmatrix} -\frac{1}{\sqrt{N_c^2-1}} & -\frac{1}{\sqrt{2}} \sqrt{\frac{N_c-2}{N_c-1}} & -\frac{1}{\sqrt{2}} \sqrt{\frac{N_c+2}{N_c+1}} \\ \frac{1}{\sqrt{2}} \sqrt{\frac{N_c}{N_c^2-1}} & \frac{1}{2} \sqrt{\frac{N_c-2}{N_c-1}} & -\frac{1}{2} \sqrt{\frac{N_c+2}{N_c+1}} \\ \frac{1}{\sqrt{2}} \sqrt{\frac{N_c^2-4}{N_c^2-1}} & -\frac{1}{2} \sqrt{\frac{N_c+2}{N_c-1}} & \frac{1}{2} \sqrt{\frac{N_c-2}{N_c+1}} \end{pmatrix}, \\ &= \begin{pmatrix} -\frac{1}{2\sqrt{2}} & -\frac{1}{2} & -\frac{\sqrt{5}}{2\sqrt{2}} \\ \frac{3}{4} & \frac{1}{2\sqrt{2}} & -\frac{\sqrt{5}}{4} \\ \frac{\sqrt{5}}{4} & -\frac{\sqrt{5}}{2\sqrt{2}} & \frac{1}{4} \end{pmatrix}. \end{aligned} \quad (\text{C13})$$

## APPENDIX D: THE FOUR-POINT WILSON LINE CORRELATOR

The quark-gluon Wilson line is built as the tensor product of a quark and a gluon Wilson line,

$$U_{qg}(0, L_\eta; \vec{x}_\perp, \vec{y}_\perp) \equiv U_F(0, L_\eta; \vec{x}_\perp) \otimes U_A(0, L_\eta; \vec{y}_\perp). \quad (\text{D1})$$

The dimension of the  $qg$  Wilson line is  $N_c d_A = 24$ . In the component form,

$$\begin{aligned} U_{qg}(0, L_\eta; \vec{x}_\perp, \vec{y}_\perp)_{\bar{c}_q, c_q} &= U_F(0, L_\eta; \vec{x}_\perp)_{\bar{c}_q, c_q} U_A(0, L_\eta; \vec{y}_\perp)_{\bar{c}_g, c_g}. \end{aligned} \quad (\text{D2})$$

The single  $qg$  Wilson line gives the amplitude of a quark-gluon state propagating through the color medium and can be related to its total cross section through the optical theorem, for which, see Ref. [29]. Here, we would like to understand the probability distribution of a quark-gluon state, so what we are interested in is the correlation function of two  $qg$  Wilson lines, i.e., the four-point function,

$$\begin{aligned}
S_{\bar{q}\bar{g}qg}(0, x^+; \vec{x}_{q,\perp}, \vec{x}_{g,\perp}, \vec{y}_{q,\perp}, \vec{y}_{g,\perp})_{\beta_1\beta_2\beta_3\beta_4; \alpha_1\alpha_2\alpha_3\alpha_4} \\
&= \langle U_F^\dagger(0, x^+; \vec{x}_{q,\perp})_{\alpha_1, \beta_1} U_A^\dagger(0, x^+; \vec{x}_{g,\perp})_{\alpha_2, \beta_2} U_F(0, x^+; \vec{y}_{q,\perp})_{\beta_3, \alpha_3} U_A(0, x^+; \vec{y}_{g,\perp})_{\beta_4, \alpha_4} \rangle_\rho, \\
&= e^{-(C_F+C_A)\xi L(0)} e^{\xi \mathcal{M}_{\bar{q}\bar{g}qg} |_{\beta_1\beta_2\beta_3\beta_4; \alpha_1\alpha_2\alpha_3\alpha_4}}, \tag{D3}
\end{aligned}$$

in which  $\xi \equiv g^4 \tilde{\mu}^2 x^+$  and

$$\begin{aligned}
-\mathcal{M}_{\bar{q}\bar{g}qg} &\equiv (-T^{a*}) \otimes I_A \otimes T^a \otimes I_A L(|\vec{x}_{q,\perp} - \vec{y}_{q,\perp}|) + I_F \otimes (-t^{a*}) \otimes I_F \otimes t^a L(|\vec{x}_{g,\perp} - \vec{y}_{g,\perp}|) \\
&\quad + (-T^{a*}) \otimes (-t^{a*}) \otimes I_F \otimes I_A L(|\vec{x}_{q,\perp} - \vec{x}_{g,\perp}|) + I_F \otimes I_A \otimes T^a \otimes t^a L(|\vec{y}_{q,\perp} - \vec{y}_{g,\perp}|) \\
&\quad + (-T^{a*}) \otimes I_A \otimes I_F \otimes t^a L(|\vec{x}_{q,\perp} - \vec{y}_{g,\perp}|) + I_F \otimes (-t^{a*}) \otimes T^a \otimes I_A L(|\vec{x}_{g,\perp} - \vec{y}_{q,\perp}|). \tag{D4}
\end{aligned}$$

The above expression gives the amplitude of a  $\bar{q}gqg$  quadruple going from color configuration  $\{\bar{c}_q = \alpha_1, \bar{c}_g = \alpha_2, c_q = \alpha_3, c_g = \alpha_4\}$  to  $\{\bar{c}_q = \beta_1, \bar{c}_g = \beta_2, c_q = \beta_3, c_g = \beta_4\}$ . This function  $S_{\bar{q}\bar{g}qg}$  is  $576 \times 576$  in the full color space of the  $\bar{q} \otimes \bar{g} \otimes q \otimes g$  state. But since we are interested in the probability of the  $qg$  state transferring from some color state  $\{c_q = \alpha_1, c_g = \alpha_2\}$  to  $\{c_q = \beta_1, c_g = \beta_2\}$ , the quantity we should look at is in the form of  $S_{\bar{q}\bar{g}qg} |_{\beta_1\beta_2\beta_1\beta_2; \alpha_1\alpha_2\alpha_1\alpha_2}$ . Therefore, we only need to study the  $\bar{q}gqg$  singlet states. A closely related study in the color structure can be found in Ref. [64], which is carried out in terms of six-point fundamental Wilson line correlators.

In the  $s$  basis as given by Eq. (C10), we have [equivalent to Eq. (49) in Ref. [64]],

$$\mathcal{M}_{\bar{q}\bar{g}qg}^s = \begin{pmatrix} \Gamma_0 & -\frac{1}{\sqrt{2}}\Gamma_2 & 0 \\ -\frac{1}{\sqrt{2}}\Gamma_2 & \frac{N_c}{4}\Gamma_1 & \frac{\sqrt{N_c C_d}}{4}\Gamma_2 \\ 0 & \frac{\sqrt{N_c C_d}}{4}\Gamma_2 & \frac{N_c}{4}\Gamma_1 \end{pmatrix}, \tag{D5}$$

where

$$\begin{aligned}
\Gamma_0 &= C_F L^{13} + N_c L_{24}, \\
\Gamma_1 &= (L_2^1 + L_4^1 + L_2^3 + L_4^3) - \frac{2}{N_c^2} L^{13} + 2L_{24}, \\
\Gamma_2 &= L_2^1 - L_4^1 - L_2^3 + L_4^3. \tag{D6}
\end{aligned}$$

For the convenience of reading, let us define a short-hand notation for the scalar function  $L(r)$ , by putting the particle index that labels the contracted quark (gluon) into the superscript (subscript),  $L_{[\text{quarks}]}$  ( $L_{[\text{gluons}]}$ ). The four particles are labeled by numbers 1 to 4 from left to right, the same order used in the color indices  $\alpha_i$  as in Eq. (D3). For example,

$$L^{13} = L(|\vec{x}_{q,\perp} - \vec{y}_{q,\perp}|), \quad L_{24} = L(|\vec{x}_{g,\perp} - \vec{y}_{g,\perp}|).$$

The four-point Wilson line correlator in the  $s$  basis reads

$$\begin{aligned}
S_{\bar{q}\bar{g}qg}^s &= e^{-(C_F+C_A)\xi L(0)} \sum_{i=1}^3 \frac{e^{-z_i \xi/4}}{d(z_i)} \\
&\quad \times \begin{pmatrix} m_{11}(z_i) & m_{12}(z_i) & m_{13}(z_i) \\ m_{21}(z_i) & m_{22}(z_i) & m_{23}(z_i) \\ m_{31}(z_i) & m_{32}(z_i) & m_{33}(z_i) \end{pmatrix}, \tag{D7}
\end{aligned}$$

in which

$$z_i = -\frac{1}{3} \left[ b + \zeta^i C + \frac{\Delta_0}{\zeta^i C} \right], \quad \zeta = \frac{-1 + i\sqrt{3}}{2}, \tag{D8}$$

the roots of characteristic polynomial  $\det(-z/4I - M_{\bar{q}\bar{g}qg}^s) = 0$ ,

$$\begin{aligned}
a &= 1, \\
b &= 2(2\Gamma_0 + N_c \Gamma_1), \\
c &= N_c \Gamma_1 (N_c \Gamma_1 + 8\Gamma_0) - (N_c^2 + 4)\Gamma_2^2, \\
d &= 4\{N_c^2 \Gamma_0 \Gamma_1^2 - [(N_c^2 - 4)\Gamma_0 + 2N_c \Gamma_1] \Gamma_2^2\}, \tag{D9}
\end{aligned}$$

the coefficients, and

$$\begin{aligned}
\Delta_0 &= b^2 - 3ac, \\
\Delta_1 &= 2b^3 - 9abc + 27a^2d, \\
C &= \sqrt[3]{\frac{\Delta_1 + \sqrt{\Delta_1^2 - 4\Delta_0^3}}{2}}. \tag{D10}
\end{aligned}$$

The matrix elements read

$$d(z_i) \equiv \prod_{\substack{j=1 \\ j \neq i}}^3 (z_i - z_j) = 3z_i^2 + 4c_1 z_i + c, \tag{D11a}$$



$$m_{11}(z_i) = (z_i + N_c \Gamma_1)^2 + (4 - N_c^2) \Gamma_2^2, \quad (\text{D11b})$$

$$m_{12}(z_i) = m_{21}(z_i) = 2\sqrt{2} \Gamma_2 (z_i + N_c \Gamma_1), \quad (\text{D11c})$$

$$m_{13}(z_i) = m_{31}(z_i) = -2\sqrt{2C_d N_c} \Gamma_2^2, \quad (\text{D11d})$$

$$m_{22}(z_i) = z_i^2 + (4\Gamma_0 + N_c \Gamma_1) z_i + 4N_c \Gamma_1 \Gamma_0, \quad (\text{D11e})$$

$$m_{23}(z_i) = m_{32}(z_i) = -\sqrt{C_d N_c} \Gamma_2 (4\Gamma_0 + z_i), \quad (\text{D11f})$$

$$m_{33}(z_i) = m_{22}(z_i) - 8\Gamma_2^2. \quad (\text{D11g})$$

We, therefore, arrive at Eq. (55) in Ref. [64]. The result is translationally invariant, which can also be seen from the definition in Eq. (D4) in the sense that it only depends on the relative positions among the four particles but not the center of mass of the system. Explicitly, we can write

$$\begin{aligned} S_{\bar{q}\bar{g}qg}(0, x^+; \vec{x}_{q,\perp}, \vec{x}_{g,\perp}, \vec{y}_{q,\perp}, \vec{y}_{g,\perp}) \\ = S_{\bar{q}\bar{g}qg}(0, x^+; \vec{x}_{q,\perp}, \vec{x}_{g,\perp}, \vec{x}_{q,\perp} - \vec{u}_{q,\perp}, \vec{x}_{g,\perp} - \vec{u}_{g,\perp}), \\ = S_{\bar{q}\bar{g}qg}(0, x^+; \vec{v}_\perp + \vec{u}_{q,\perp}, \vec{u}_{q,\perp}, \vec{v}_\perp, \vec{u}_{q,\perp} - \vec{u}_{g,\perp}). \end{aligned} \quad (\text{D12})$$

In the second line, we make the change of variables according to Eq. (24); in the third line, we shift all the four position arguments by  $-\vec{x}_{g,\perp} + \vec{u}_{g,\perp}$ . This rewriting is for the convenience of identifying the relevant physical quantities, without making any actual change to the content. Let us also write out  $\Gamma$ s defined in Eq. (D6) in terms of the three independent vectors  $\vec{v}_\perp$ ,  $\vec{u}_{q,\perp}$ , and  $\vec{u}_{g,\perp}$ ,

$$\begin{aligned} \Gamma_0 &= C_F L(u_{q,\perp}) + N_c L(u_{g,\perp}), \\ \Gamma_1 &= (L(v_\perp) + L(|\vec{v}_\perp + \vec{u}_{g,\perp}|) + L(|\vec{v}_\perp - \vec{u}_{q,\perp}|) \\ &\quad + L(|\vec{v}_\perp - \vec{u}_{q,\perp} + \vec{u}_{g,\perp}|)) - \frac{2}{N_c^2} L(u_{q,\perp}) + 2L(u_{g,\perp}), \\ \Gamma_2 &= L(v_\perp) - L(|\vec{v}_\perp + \vec{u}_{g,\perp}|) - L(|\vec{v}_\perp - \vec{u}_{q,\perp}|) \\ &\quad + L(|\vec{v}_\perp - \vec{u}_{q,\perp} + \vec{u}_{g,\perp}|). \end{aligned} \quad (\text{D13})$$

We denote the modulus of a vector using the same variable without the arrow,  $u_l = |\vec{u}_l|$ .

Knowing the explicit form of  $S_{\bar{q}\bar{g}qg}^s$ , we can now evaluate the probability function of a quark-gluon state. In doing so, we interpret the  $\bar{q}\bar{g}qg$  state as a  $qg$  state and its conjugate. Consider a quark-gluon state in a gauge-invariant color space  $c$  with dimension  $d_c$ , then the corresponding  $\bar{q}\bar{g}qg$  state is in the color configuration  $\bar{c}c$ . The color space  $c$  could be the 3, the  $\bar{6}$ , the 15, and the full  $N_c d_A$  space denoted by ‘‘X.’’ The first three cases correspond to the three  $v$ -basis states, and the last one the  $|s_1\rangle$  state. The initial state is averaged over the corresponding  $qg$  color space,

$$\begin{aligned} &|\Psi_{\bar{q}\bar{g}qg, \bar{c}_i(\bar{q}\bar{g})c_i(qg)}\rangle \\ &= \frac{1}{d_c} |\bar{\Psi}_{qg, c_i}\rangle \otimes |\Psi_{qg, c_i}\rangle \\ &= \begin{cases} \frac{1}{\sqrt{\dim(R_i)}} |v_i\rangle, & c_i = 3, \bar{6}, 15 \\ -\frac{1}{\sqrt{N_c d_A}} |s_1\rangle, & c_i = X \end{cases}. \end{aligned} \quad (\text{D14})$$

The final state is summed over the corresponding  $qg$  color space,

$$\begin{aligned} &|\Psi_{\bar{q}\bar{g}qg, \bar{c}_f(\bar{q}\bar{g})c_f(qg)}\rangle \\ &= d_c |\bar{\Psi}_{qg, c_f}\rangle \otimes |\Psi_{qg, c_f}\rangle, \\ &= \begin{cases} \sqrt{\dim(R_f)} |v_f\rangle, & c_f = 3, \bar{6}, 15 \\ -\sqrt{N_c d_A} |s_1\rangle, & c_f = X \end{cases}. \end{aligned} \quad (\text{D15})$$

The probability function of a  $qg$  state is, therefore, from one color subspace to the other,

$$\begin{aligned} \mathcal{P}_{qg, c_i \rightarrow c_f} &\equiv \langle \Psi_{\bar{q}\bar{g}qg, \bar{c}_f(\bar{q}\bar{g})c_f(qg)} | S_{\bar{q}\bar{g}qg} | \Psi_{\bar{q}\bar{g}qg, \bar{c}_i(\bar{q}\bar{g})c_i(qg)} \rangle, \\ &= \frac{\sqrt{\dim(R_f)}}{\sqrt{\dim(R_i)}} \langle v_f | S_{\bar{q}\bar{g}qg} | v_i \rangle, \end{aligned} \quad (\text{D16})$$

and from one color subspace to the full space,

$$\begin{aligned} \mathcal{P}_{qg, c} &\equiv \sum_{i=1}^{N_c} \sum_{a=1}^{d_A} \langle \Psi_{\bar{q}\bar{g}qg, \{i, a, i, a\}} | S_{\bar{q}\bar{g}qg} | \Psi_{\bar{q}\bar{g}qg, \bar{c}(\bar{q}\bar{g})c(qg)} \rangle, \\ &= -\sqrt{N_c d_A} \langle s_1 | S_{\bar{q}\bar{g}qg} | \Psi_{\bar{q}\bar{g}qg, \bar{c}(\bar{q}\bar{g})c(qg)} \rangle. \end{aligned} \quad (\text{D17})$$

The relation between the color-differential and the color-inclusive cross sections is

$$\mathcal{P}_{qg, c_i} = \mathcal{P}_{qg, c_i \rightarrow X} = \sum_{c_f=3, \bar{6}, 15} \mathcal{P}_{qg, c_i \rightarrow c_f}. \quad (\text{D18})$$

In analogy, the relation between the cross sections of the color-differential and the color-inclusive incoming states is

$$N_c d_A \mathcal{P}_{qg, X \rightarrow c_f} = \sum_{c_f=3, \bar{6}, 15} \dim(R_i) \mathcal{P}_{qg, c_i \rightarrow c_f}. \quad (\text{D19})$$

The probability function in the full-color space is

$$\mathcal{P}_{qg, X} = \langle s_1 | S_{\bar{q}\bar{g}qg} | s_1 \rangle = S_{11}^s. \quad (\text{D20})$$

The probability function of the triplet is

$$\mathcal{P}_{qg, 3} = S_{11}^s - \frac{N_c \sqrt{2}}{2} S_{12}^s - \frac{\sqrt{2(N_c^2 - 4)}}{2} S_{13}^s. \quad (\text{D21})$$

The color differential probability is

$$\begin{aligned}
\mathcal{P}_{qg,3\rightarrow 3} &= \frac{1}{2(N_c^2 - 1)} \left[ 2S_{11}^s - 2\sqrt{2}N_c S_{12}^s - 2\sqrt{2(N_c^2 - 4)}S_{13}^s + N_c^2 S_{22}^s + 2N_c\sqrt{N_c^2 - 4}S_{23}^s + (N_c^2 - 4)S_{33}^s \right], \\
\mathcal{P}_{qg,3\rightarrow \bar{6}} &= \frac{1}{4(N_c - 1)} \left[ 2(N_c - 2)S_{11}^s - (N_c + 1)(N_c - 2)\sqrt{2}S_{12}^s - (N_c - 3)\sqrt{2(N_c^2 - 4)}S_{13}^s \right. \\
&\quad \left. + N_c(N_c - 2)S_{22}^s - 2\sqrt{N_c^2 - 4}S_{23}^s - (N_c + 2)(N_c - 2)S_{33}^s \right], \\
\mathcal{P}_{qg,3\rightarrow 15} &= \frac{1}{4(N_c + 1)} \left[ 2(N_c + 2)S_{11}^s - (N_c - 1)(N_c + 2)\sqrt{2}S_{12}^s - (N_c + 3)\sqrt{2(N_c^2 - 4)}S_{13}^s - N_c(N_c + 2)S_{22}^s \right. \\
&\quad \left. + 2\sqrt{N_c^2 - 4}S_{23}^s + (N_c + 2)(N_c - 2)S_{33}^s \right]. \tag{D22}
\end{aligned}$$

The probability function of the  $\bar{6}$  is

$$\mathcal{P}_{qg,\bar{6}} = S_{11}^s - \frac{\sqrt{2}}{2}S_{12}^s + \sqrt{\frac{N_c + 2}{2(N_c - 2)}}S_{13}^s, \tag{D23}$$

and color differentially,

$$\begin{aligned}
\mathcal{P}_{qg,\bar{6}\rightarrow 3} &= \frac{\dim(3)}{\dim(\bar{6})}\mathcal{P}_{qg,3\rightarrow \bar{6}}, \\
\mathcal{P}_{qg,\bar{6}\rightarrow \bar{6}} &= \frac{1}{4(N_c - 1)} \left[ 2(N_c - 2)S_{11}^s - 2\sqrt{2}(N_c - 2)S_{12}^s + 2\sqrt{2(N_c^2 - 4)}S_{13}^s + (N_c - 2)S_{22}^s \right. \\
&\quad \left. - 2\sqrt{N_c^2 - 4}S_{23}^s + (N_c + 2)S_{33}^s \right], \\
\mathcal{P}_{qg,\bar{6}\rightarrow 15} &= \frac{1}{4(N_c + 1)}\sqrt{\frac{N_c + 2}{N_c - 2}} \left[ 2\sqrt{N_c^2 - 4}S_{11}^s + 4\sqrt{2}S_{13}^s - \sqrt{N_c^2 - 4}S_{22}^s + 2N_c S_{23}^s - \sqrt{N_c^2 - 4}S_{33}^s \right]. \tag{D24}
\end{aligned}$$

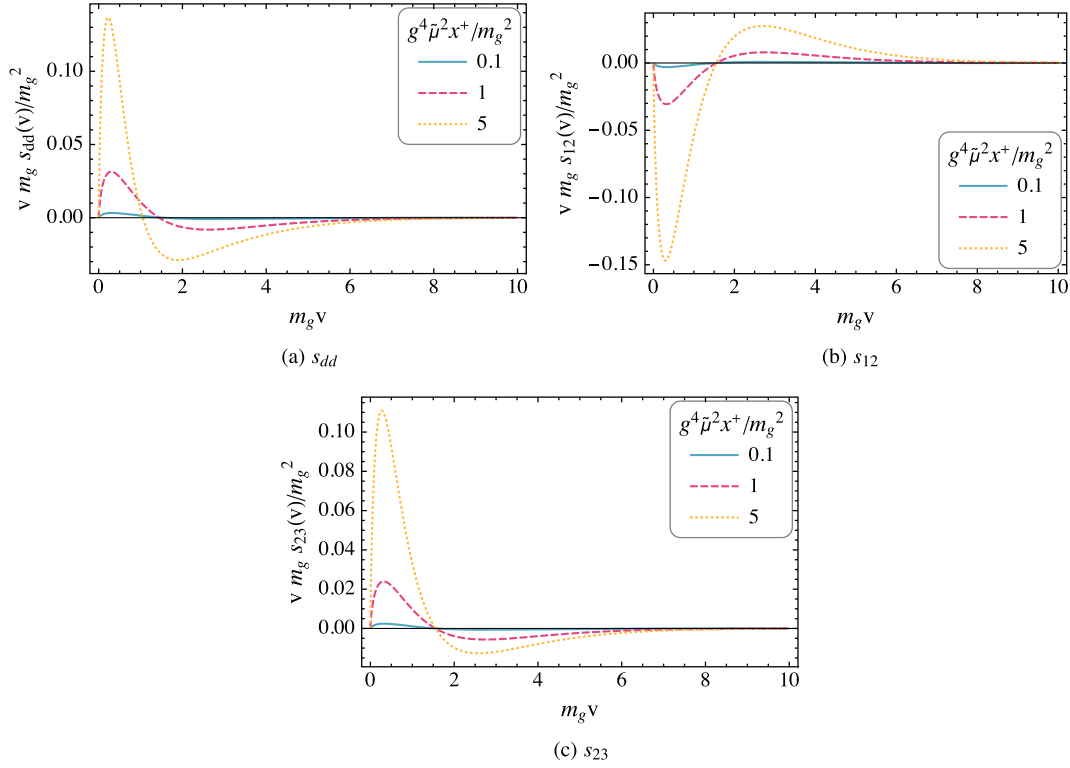
The probability function of the 15-plet is

$$\mathcal{P}_{qg,15} = S_{11}^s + \frac{\sqrt{2}}{2}S_{12}^s - \sqrt{\frac{N_c - 2}{2(N_c + 2)}}S_{13}^s \tag{D25}$$

and

$$\begin{aligned}
\mathcal{P}_{qg,15\rightarrow 3} &= \frac{\dim(3)}{\dim(15)}\mathcal{P}_{qg,3\rightarrow 15}, \\
\mathcal{P}_{qg,15\rightarrow \bar{6}} &= \frac{\dim(\bar{6})}{\dim(15)}\mathcal{P}_{qg,\bar{6}\rightarrow 15}, \\
\mathcal{P}_{qg,15\rightarrow 15} &= \frac{1}{4(N_c + 1)} \left[ 2(N_c + 2)S_{11}^s + 2\sqrt{2}(N_c + 2)S_{12}^s - 2\sqrt{2(N_c^2 - 4)}S_{13}^s + (N_c + 2)S_{22}^s \right. \\
&\quad \left. - 2\sqrt{N_c^2 - 4}S_{23}^s + (N_c - 2)S_{33}^s \right]. \tag{D26}
\end{aligned}$$

We have written above the color-differential and inclusive probability functions  $\mathcal{P}_{qg}$  in terms of the components of  $S_{\bar{q}\bar{g}qg}^s$ . In the dilute limit, one can replace  $S_{\bar{q}\bar{g}qg}^s$  by its exponent  $\mathcal{M}_{\bar{q}\bar{g}qg}^s$  as given in Eq. (D5). Then the probability function can be written in terms of the dipole cross sections  $L^{13}, L_{24}, \dots$ ; see discussion in Ref. [76] in the context of quark-gluon dijet


 FIG. 21. Plot of  $vs_{mn}(v)$  ( $mn = dd, 12, 23$ ) as a function of  $v$  according to Eq. (D29).

production off nuclei. The curious  $N_c \rightarrow -N_c$  symmetry between the  $\bar{6}$  and 15 states is observed here as

$$\mathcal{P}_{qg,3 \rightarrow \bar{6}}(N_c) = -\mathcal{P}_{qg,3 \rightarrow 15}(-N_c), \quad (\text{D27a})$$

$$\mathcal{P}_{qg,\bar{6} \rightarrow \bar{6}}(N_c) = -\mathcal{P}_{qg,15 \rightarrow 15}(-N_c), \quad (\text{D27b})$$

by noting that  $\mathcal{M}_{ii}^s(N_c) = -\mathcal{M}_{ii}^s(-N_c)$ ,  $i = 1, 2, 3$  according to Eq. (D5).

Then, the derivative is

$$\lim_{\vec{u}_{g,\perp}, \vec{u}_{q,\perp} \rightarrow \vec{0}_\perp} \vec{\nabla}_{u,q} \cdot \vec{\nabla}_{u,g} \mathcal{S}_{\bar{q}gqg}^s = \begin{pmatrix} 0 & s_{12}(v) & 0 \\ s_{12}(v) & s_{dd}(v) & s_{23}(v) \\ 0 & s_{23}(v) & s_{dd}(v) \end{pmatrix}, \quad (\text{D28})$$

in which

$$\begin{aligned} \tilde{\alpha}_1 &= 4N_c[L(0) - L(v)], \\ s_{dd}(v) &= -\nabla_v^2 L(v) \frac{N_c \xi}{4} e^{-\xi \tilde{\alpha}_1/4} - [L'(v)]^2 \frac{N_c^2 \xi^2}{4} e^{-\xi \tilde{\alpha}_1/4}, \\ s_{12}(v) &= -\nabla_v^2 L(v) \frac{2\sqrt{2}}{\tilde{\alpha}_1} [e^{-\xi \tilde{\alpha}_1/4} - 1], \\ s_{23}(v) &= -\nabla_v^2 L(v) \frac{\sqrt{C_d N_c}}{4} e^{-\xi \tilde{\alpha}_1/4} \xi. \end{aligned} \quad (\text{D29})$$

In the quark-gluon coincidence limit,

$$\begin{aligned} \lim_{v \rightarrow 0} s_{dd}(v) &= \frac{N_c}{4} \xi \mathcal{G}_2, \\ \lim_{v \rightarrow 0} s_{12}(v) &= -\frac{\sqrt{2}}{2} \xi \mathcal{G}_2, \\ \lim_{v \rightarrow 0} s_{23}(v) &= \frac{\sqrt{C_d N_c}}{4} \xi \mathcal{G}_2. \end{aligned} \quad (\text{D30})$$

It is straightforward to verify that, in the  $v \rightarrow 0$  limit, the total momentum of the quark-gluon system behaves as a single particle in the corresponding color representation  $c$ ,

$$\lim_{v \rightarrow 0} (\vec{p}_{q,\perp} + \vec{p}_{g,\perp})^2|_{qg,c} = C_c \mathcal{G}_2 \xi, \quad (\text{D31})$$

in which  $C_c$  is the corresponding Casimir, and specially  $C_X = C_3 + C_8$  for color-uncorrelated state for which the cross term  $\vec{p}_{q,\perp} \cdot \vec{p}_{g,\perp}$  vanishes. The total momentum can be calculated as

$$\begin{aligned} &(\vec{p}_{q,\perp} + \vec{p}_{g,\perp})^2|_{qg,c} \\ &= \lim_{\vec{u}_{g,\perp}, \vec{u}_{q,\perp} \rightarrow \vec{0}_\perp} -(\vec{\nabla}_{u,q}^2 + \vec{\nabla}_{u,g}^2 + 2\vec{\nabla}_{u,q} \cdot \vec{\nabla}_{u,g}) \mathcal{P}_{qg,c}. \end{aligned} \quad (\text{D32})$$

To compute the momentum broadening for a quark-gluon state in general, the next step is to integrate over  $\vec{v}$  as shown in Eq. (27),

$$\int_{\vec{v}} f_{\text{Rel}}(\vec{v}_{\perp}) \vec{\nabla}_{u,q} \cdot \vec{\nabla}_{u,g} \mathcal{P}_{qg,c}(0, x^+; \vec{v}_{\perp} + \vec{u}_{q,\perp}, \vec{u}_{q,\perp}, \vec{v}_{\perp}, \vec{u}_{q,\perp} - \vec{u}_{g,\perp})|_{\vec{u}_{q,\perp}, \vec{u}_{g,\perp} = \vec{0}_{\perp}}. \quad (\text{D33})$$

All three nonvanishing elements exhibit a logarithmic divergence at  $v = 0$ , as indicated by the  $\mathcal{G}_2$  in Eq. (D30). We present the behavior of those elements multiplied by  $v$  in Fig. 21. In the plots, we take a dimensionless quantity  $vm_g$ , such that we are looking at the quark-gluon separation in units of  $1/m_g$ .

- 
- [1] W. Busza, K. Rajagopal, and W. van der Schee, *Annu. Rev. Nucl. Part. Sci.* **68**, 339 (2018).
- [2] I. Arsene *et al.* (BRAHMS Collaboration), *Nucl. Phys.* **A757**, 1 (2005).
- [3] B. B. Back *et al.* (PHOBOS Collaboration), *Nucl. Phys.* **A757**, 28 (2005).
- [4] J. Adams *et al.* (STAR Collaboration), *Nucl. Phys.* **A757**, 102 (2005).
- [5] K. Adcox *et al.* (PHENIX Collaboration), *Nucl. Phys.* **A757**, 184 (2005).
- [6] G. Aad *et al.* (ATLAS Collaboration), *Phys. Rev. Lett.* **105**, 252303 (2010).
- [7] K. Aamodt *et al.* (ALICE Collaboration), *Phys. Lett. B* **696**, 30 (2011).
- [8] S. Chatrchyan *et al.* (CMS Collaboration), *Phys. Rev. C* **84**, 024906 (2011).
- [9] R. Baier, *Nucl. Phys.* **A715**, 209 (2003).
- [10] J. Casalderrey-Solana and C. A. Salgado, *Acta Phys. Pol. B* **38**, 3731 (2007).
- [11] D. d'Enterria, *Landolt-Bornstein* **23**, 471 (2010).
- [12] A. Majumder and M. Van Leeuwen, *Prog. Part. Nucl. Phys.* **66**, 41 (2011).
- [13] G.-Y. Qin and X.-N. Wang, *Int. J. Mod. Phys. E* **24**, 1530014 (2015).
- [14] S. Cao and X.-N. Wang, *Rep. Prog. Phys.* **84**, 024301 (2021).
- [15] L. Apolinário, Y.-J. Lee, and M. Winn, *Prog. Part. Nucl. Phys.* **127**, 103990 (2022).
- [16] R. Baier, Y. L. Dokshitzer, A. H. Mueller, S. Peigne, and D. Schiff, *Nucl. Phys.* **B483**, 291 (1997).
- [17] R. Baier, Y. L. Dokshitzer, A. H. Mueller, S. Peigne, and D. Schiff, *Nucl. Phys.* **B484**, 265 (1997).
- [18] B. G. Zakharov, *JETP Lett.* **65**, 615 (1997).
- [19] M. Gyulassy, P. Levai, and I. Vitev, *Nucl. Phys.* **B571**, 197 (2000).
- [20] M. Gyulassy, P. Levai, and I. Vitev, *Phys. Rev. Lett.* **85**, 5535 (2000).
- [21] U. A. Wiedemann, *Nucl. Phys.* **B588**, 303 (2000).
- [22] P. B. Arnold, G. D. Moore, and L. G. Yaffe, *J. High Energy Phys.* **11** (2001) 057.
- [23] P. B. Arnold, G. D. Moore, and L. G. Yaffe, *J. High Energy Phys.* **06** (2002) 030.
- [24] X.-f. Guo and X.-N. Wang, *Phys. Rev. Lett.* **85**, 3591 (2000).
- [25] X.-N. Wang and X.-f. Guo, *Nucl. Phys.* **A696**, 788 (2001).
- [26] G. Ovanessian and I. Vitev, *Phys. Lett. B* **706**, 371 (2012).
- [27] G. Ovanessian and I. Vitev, *J. High Energy Phys.* **06** (2011) 080.
- [28] M. Li, X. Zhao, P. Maris, G. Chen, Y. Li, K. Tuchin, and J. P. Vary, *Phys. Rev. D* **101**, 076016 (2020).
- [29] M. Li, T. Lappi, and X. Zhao, *Phys. Rev. D* **104**, 056014 (2021).
- [30] J. P. Vary, H. Honkanen, J. Li, P. Maris, S. J. Brodsky, A. Harindranath, G. F. de Teramond, P. Sternberg, E. G. Ng, and C. Yang, *Phys. Rev. C* **81**, 035205 (2010).
- [31] X. Zhao, A. Ilderton, P. Maris, and J. P. Vary, *Phys. Rev. D* **88**, 065014 (2013).
- [32] G. Chen, X. Zhao, Y. Li, K. Tuchin, and J. P. Vary, *Phys. Rev. D* **95**, 096012 (2017).
- [33] B. Hu, A. Ilderton, and X. Zhao, *Phys. Rev. D* **102**, 016017 (2020).
- [34] Z. Lei, B. Hu, and X. Zhao, [arXiv:2201.01746](https://arxiv.org/abs/2201.01746).
- [35] W. Du, P. Yin, Y. Li, G. Chen, W. Zuo, X. Zhao, and J. P. Vary, *Phys. Rev. C* **97**, 064620 (2018).
- [36] P. Yin, W. Du, W. Zuo, X. Zhao, and J. P. Vary, [arXiv:2208.00267](https://arxiv.org/abs/2208.00267).
- [37] M. Li, [arXiv:2304.12842](https://arxiv.org/abs/2304.12842).
- [38] W. Du, J. P. Vary, X. Zhao, and W. Zuo, *Phys. Rev. A* **104**, 012611 (2021).
- [39] J. a. Barata, X. Du, M. Li, W. Qian, and C. A. Salgado, *Phys. Rev. D* **106**, 074013 (2022).
- [40] X. Yao, [arXiv:2205.07902](https://arxiv.org/abs/2205.07902).
- [41] J. Barata, X. Du, M. Li, W. Qian, C. A. Salgado, [arXiv:2307.01792](https://arxiv.org/abs/2307.01792).
- [42] F. Arute *et al.*, *Nature (London)* **574**, 505 (2019).
- [43] J. W. Z. Lau, K. H. Lim, H. Shrotriya, and L. C. Kwek, *AAPPS Bull.* **32**, 27 (2022).
- [44] L. D. McLerran and R. Venugopalan, *Phys. Rev. D* **49**, 2233 (1994).
- [45] L. D. McLerran and R. Venugopalan, *Phys. Rev. D* **49**, 3352 (1994).
- [46] L. D. McLerran and R. Venugopalan, *Phys. Rev. D* **50**, 2225 (1994).
- [47] N. N. Nikolaev, W. Schafer, B. G. Zakharov, and V. R. Zoller, *J. Exp. Theor. Phys.* **97**, 441 (2003).
- [48] F. Dominguez, C. Marquet, A. M. Stasto, and B.-W. Xiao, *Phys. Rev. D* **87**, 034007 (2013).
- [49] L. Apolinário, N. Armesto, J. G. Milhano, and C. A. Salgado, *J. High Energy Phys.* **02** (2015) 119.
- [50] J.-P. Blaizot, F. Dominguez, E. Iancu, and Y. Mehtar-Tani, *J. High Energy Phys.* **06** (2014) 075.

- [51] K. Boguslavski, A. Kurkela, T. Lappi, F. Lindenbauer, and J. Peuron, [arXiv:2303.12595](https://arxiv.org/abs/2303.12595).
- [52] T. Lappi, *Eur. Phys. J. C* **55**, 285 (2008).
- [53] T. Altinoluk, N. Armesto, G. Beuf, M. Martínez, and C. A. Salgado, *J. High Energy Phys.* **07** (2014) 068.
- [54] P. Agostini, T. Altinoluk, N. Armesto, F. Dominguez, and J. G. Milhano, *Eur. Phys. J. C* **82**, 1001 (2022).
- [55] P. Agostini, T. Altinoluk, and N. Armesto, *Phys. Lett. B* **840**, 137892 (2023).
- [56] E. Braaten and R. D. Pisarski, *Nucl. Phys.* **B337**, 569 (1990).
- [57] M. Gyulassy and X.-n. Wang, *Nucl. Phys.* **B420**, 583 (1994).
- [58] Y. Mehtar-Tani, J. G. Milhano, and K. Tywoniuk, *Int. J. Mod. Phys. A* **28**, 1340013 (2013).
- [59] J. a. Barata, Y. Mehtar-Tani, A. Soto-Ontoso, and K. Tywoniuk, *Phys. Rev. D* **104**, 054047 (2021).
- [60] A. Kovner and U. A. Wiedemann, *Quark–Gluon Plasma 3* (World Scientific Publishing, Singapore, 2004), pp. 192–248, [10.1142/9789812795533\\_0004](https://arxiv.org/abs/10.1142/9789812795533_0004).
- [61] H. Liu, K. Rajagopal, and U. A. Wiedemann, *Phys. Rev. Lett.* **97**, 182301 (2006).
- [62] A. Majumder, *Phys. Rev. C* **87**, 034905 (2013).
- [63] M. Benzke, N. Brambilla, M. A. Escobedo, and A. Vairo, *J. High Energy Phys.* **02** (2013) 129.
- [64] T. Lappi, H. Mäntysaari, and A. Ramnath, *Phys. Rev. D* **102**, 074027 (2020).
- [65] J.-P. Blaizot, F. Dominguez, E. Iancu, and Y. Mehtar-Tani, *J. High Energy Phys.* **01** (2013) 143.
- [66] T. Liou, A. H. Mueller, and B. Wu, *Nucl. Phys.* **A916**, 102 (2013).
- [67] Y.-Y. Zhang and X.-N. Wang, *Phys. Rev. D* **105**, 034015 (2022).
- [68] S. J. Brodsky, H.-C. Pauli, and S. S. Pinsky, *Phys. Rep.* **301**, 299 (1998).
- [69] M. D. Schwartz, *Quantum Field Theory and the Standard Model* (Cambridge University Press, Cambridge, England, 2014).
- [70] F. Cougoulic and Y. V. Kovchegov, *Nucl. Phys.* **A1004**, 122051 (2020).
- [71] H. Georgi, *Lie Algebras In Particle Physics: From Isospin To Unified Theories* (Taylor & Francis, Boca Raton, 2000).
- [72] SU(N) Clebsch-Gordan coefficients generator, <https://homepages.physik.uni-muenchen.de/~7Evondelft/Papers/ClebschGordan/>.
- [73] A. Alex, M. Kalus, A. Huckleberry, and J. von Delft, *J. Math. Phys. (N.Y.)* **52**, 023507 (2011).
- [74] F. Cougoulic, Nuclear effects in high-energy proton-nucleus collisions: Transverse momentum broadening of energetic parton systems and soft anomalous dimension matrices, theses, Ecole nationale supérieure Mines-Télécom Atlantique, 2018, <https://inspirehep.net/files/b0f83265efdfcd75fa9c10fa7fd4181c>.
- [75] F. Cougoulic (personal communication).
- [76] N. N. Nikolaev, W. Schafer, B. G. Zakharov, and V. R. Zoller, *Phys. Rev. D* **72**, 034033 (2005).